Received: 27 February 2018 | Revised: 22 November 2018 | Accepted: 26 November 2018 | Published on: 4 February 2019

DOI: 10.1002/qj.3453

RESEARCH ARTICLE

Quarterly Journal of the Royal Meteorological Society RMetS

The asymmetric eddy–background flow interaction in the North Pacific storm track

Yuan-Bing Zhao[1] | X. San Liang[1,2] | Zhaoyong Guan[1] | Kevin I. Hodges[3]

[1]School of Atmospheric Sciences, Nanjing University of Information Science and Technology, Nanjing, China
[2]School of Marine Sciences, Nanjing University of Information Science and Technology, Nanjing, China
[3]Department of Meteorology, National Centre for Earth Observation, University of Reading, Reading, UK

Correspondence
X. San Liang, Nanjing Center for Ocean-Atmosphere Dynamical Studies, Nanjing, Jiangsu 210044, China.
Email: x.san.liang@gmail.com

Funding information
National Program on Global Change and Air-Sea Interaction, GASI-IPOVAI-06. 2015 Jiangsu Chair Professorship. 2015 Jiangsu Program for Innovation Research and Entrepreneurship Groups. National Natural Science Foundation of China, 41276032, 41705024. NERC National Centre for Atmospheric Science (NCAS).

Using a recently developed methodology, namely the multiscale window transform (MWT) and the MWT-based theory of canonical transfer and localized multiscale energetics analysis, we investigate in an eddy-following way the nonlinear eddy–background flow interaction in the North Pacific storm track, based on the ERA-40 reanalysis data from the European Centre for Medium-Range Weather Forecasts. It is found that more than 50% of the storms occur on the northern flank of the jet stream, about 40% are around the jet centre, and very few (less than 5%) happen on the southern flank. For storms near or to the north of the jet centre, their interaction with the background flow is asymmetric in latitude. In higher latitudes, strong downscale canonical available potential energy transfer happens, especially in the mid-troposphere, which reduces the background baroclinicity and decelerates the jet; in lower latitudes, upscale canonical kinetic energy transfer intensifies at the jet centre, accelerating the jet and enhancing the middle-level baroclinicity. The resultant effect is that the jet strengthens but narrows, leading to an anomalous dipolar pattern in the fields of background wind and baroclinicity. For the storms on the southern side of the jet, the baroclinic canonical transfer is rather weak. On average, the local interaction begins about 3 days before a storm arrives at the site of observation, achieves its maximum as the storm arrives, and then weakens.

KEYWORDS
canonical energy transfer, eddy–mean flow interaction, extratropical cyclone, feature tracking, multiscale energetics

1 | INTRODUCTION

Eddy–mean flow interaction is one of the central issues in dynamical meteorology. In the atmosphere, a typical site of eddy–mean flow interaction is the midlatitude storm track (Blackmon, 1976; Hoskins and Valdes, 1990; Chang and Orlanski, 1993). It has been shown that the atmospheric storm track generally coincides with the tropospheric jet, where the baroclinicity is the strongest (e.g., Chang *et al.,* 2002; Lee and Kim, 2003). Within the storm track, synoptic eddies are often generated in the jet and then interact with it.

There is a long history of studies on the interaction between midlatitude synoptic eddies and the jet stream. In most early studies, the focus was on the theoretical aspects based on idealized models, such as those with small-amplitude perturbations in the form of sinusoidal waves and a zonally homogeneous, stationary background flow (in many cases also meridionally independent) (Charney and Drazin, 1961; Eliassen and Palm, 1961; Lindzen and Holton, 1968; Dickinson, 1969; Andrews and McIntyre, 1978; Plumb, 1985). However, in the real atmosphere the background flow is by nature temporally varying and zonally asymmetric, particularly in midlatitudes due to the large-scale topography and land–sea contrasts (e.g., Lee and Kim, 2003; Li and Wettstein, 2011), whilst the eddies are rather localized in space and time with finite amplitudes (Simmons and Hoskins, 1978; Blackmon *et al.,* 1984; Lim and Wallace, 1991; Chang, 1993; Catto *et al.,* 2010). In more recent studies, with the advent of observational and reanalysis data, discrepancies have been found between the previously proposed theories and the observations. For example, based on previous theories it is supposed that the baroclinic energy transfer associated with baroclinic

instability is bottom-trapped (Green, 1960; Edmon *et al.,* 1980; Lindzen and Farrell, 1980; Hoskins *et al.,* 1985; Pierrehumbert and Swanson, 1995), whereas observational energetics diagnostics have implied that midlatitude synoptic systems have their maximum baroclinic energy transfer in middle levels (e.g., Chang *et al.,* 2002). The spatial structure of the interaction is still a problem yet to be explored.

During the past two decades, eddy–mean flow interaction has been extensively discussed, especially in studies of annular modes (Robinson, 2000; Lorenz and Hartmann, 2001; Gerber and Vallis, 2007; Chen and Plumb, 2009; Kidston *et al.,* 2010; Barnes and Hartmann, 2011; Kidston and Vallis, 2012; Zhang *et al.,* 2012; Lorenz, 2014; Burrows *et al.,* 2017, to name but a few). Most of these studies have, however, focused on the zonal mean and climatologically statistical aspects. Rarely considered is the interaction between a typical individual eddy and the mean flow, except in a few studies such as that of Gerber and Vallis (2007), who argued that if the eddy is generated in the jet, the vertical wind shear is first reduced by the heat flux in the baroclinic development stage, and then in the decaying stage the jet is strengthened by upgradient momentum transfer through the wave meridional propagation (the net propagation of baroclinic wave activity away from the jet leads to momentum fluxes in the jet). On the whole, the jet structure is maintained in the presence of surface friction. Alternatively, if the eddy is growing on the shoulders of the jet, the baroclinic development stage is similar to that of the eddy growing in the jet. However, the meridional wave propagation is then limited aloft, and, as a result, the shear is reduced locally rather than over the entire baroclinic zone. Similar studies are also reported in Zhang *et al.* (2012) based on an idealized β-plane quasi-geostrophic model. As noted by Vallis and Gerber (2008), the applicability of these results to the real atmosphere still needs verification.

We remark that a classical way to look at the eddy–mean flow interaction is with the "barotropic generation rate" (Mak and Cai, 1989; Cai and Mak, 1990; Rivière *et al.,* 2003) and the "baroclinic generation rate" (Cai and Mak, 1990; Rivière *et al.,* 2004). The merit of this method is that if the eddy structure, the deformation of the jet and the positional relationship between the eddy and the jet are known, then the energy exchange between the jet and the eddy can be easily determined (especially with the barotropic generation rate). But here this method is difficult to apply, as it is derived in the quasi-geostrophic framework with the small-amplitude assumption; besides, it does not explain how eddies would modify the mean flow.

In this study we apply a newly developed methodology, which is capable of handling these nonlinear problems in a generic sense in order to diagnose the two-way interactions between individual midlatitude synoptic eddies and the background flow in an eddy-following way, in the hope of unravelling what is really happening locally in the North Pacific storm track. The methodology includes a functional analysis apparatus, namely the multiscale window transform (MWT; Liang and Anderson, 2007) and the MWT-based localized multiscale energy and vorticity analysis (MS-EVA; Liang, 2016).

The rest of this paper is organized as follows. Section 2 describes the data used in this study. In Section 3, we briefly introduce the MWT, MS-EVA and the Lagrangian tracking and compositing method, and in Section 4 we set up the MS-EVA application with the data. In the following sections (Sections 5–8), the composite reconstructed fields and a detailed eddy–mean flow interaction analysis are presented. The study is summarized in Section 9.

2 | DATA

We use for our study the 40-year European Centre for Medium-Range Weather Forecasts (ECMWF) Reanalysis (ERA-40) dataset (Uppala *et al.,* 2005), which is constrained by observations using a three-dimensional variational (3D-Var) data assimilation system. It has been used because of its length (45 years), spatial resolution (approximately $1.1° \times 1.1°$ in the tropics (T159), 35 vertical levels below 100 hPa) and temporal resolution (6 hr). More information can be found at http://apps.ecmwf.int/datasets/data/era40-daily/levtype=pl/. Here we need the velocity components (u, v and ω), the geopotential ϕ and the temperature T for the whole period from September 1957 to July 2002.

3 | METHODOLOGY

3.1 | Localized multiscale energetics analysis

The major research methodology for this study is the multiscale window transform (MWT) by Liang and Anderson (2007) and the MWT-based theory of canonical transfer (Liang, 2016) as well as the localized multiscale energy and vorticity analysis (MS-EVA) by Liang and Robinson (2005), which has been applied successfully in many atmosphere–ocean problems (e.g., Ma and Liang, 2017; Xu and Liang, 2017). This section is just a short introduction of the concepts; more details are furnished in the Appendix. For a recently updated comprehensive introduction, refer to Liang (2016).

The MWT is a functional analysis tool that helps to decompose a function space into a direct sum of several mutually orthogonal subspaces, each with an exclusive range of time scales, while preserving its local properties. Such a subspace is termed a *scale window* or simply a *window*. One may have as many windows as needed. In this study, we mainly use two, namely a low-frequency basic-flow window (or background flow window) and a synoptic-scale window (or transient window); we will also use a three-window decomposition for testing purposes. For easy reference, they are denoted and will be referred to as windows $\varpi = 0, 1, \ldots$. Given a time

series $T(t)$ with N steps, application of MWT yields two types of quantities: one is the MWT transform coefficients $\widehat{T}_n^{\sim\varpi}$ ($n = 1, 2, \ldots, N$, corresponding to the time location in t), while the other is the multiscale window reconstruction (MWR) $T^{\sim\varpi}(t)$. $T^{\sim\varpi}(t)$ is just like the low-/high-pass filtered quantity. For example, in the two-window decomposition in this study, the series $T(t)$ is decomposed into $T = T^{\sim 0}(t) + T^{\sim 1}(t)$, where $T^{\sim 0}$ stands for the background field, and $T^{\sim 1}$ is the transient (or synoptic) eddy field. MWT and MWR form a transform–reconstruction pair but they are distinctly different concepts, with the former defined in phase space and the latter in physical space (here t), just like the Fourier transform and the inverse Fourier transform. The MWR of $T(t)$ on the synoptic-scale window, for example, corresponds to a high-pass filtered signal. The lack of the transform coefficient $\widehat{T}_n^{\sim\varpi}$ in traditional filters makes it impossible to represent multiscale energy.[1] The common practice of simply taking the multiscale energy as the square of filtered variables is a conceptual mistake which, unfortunately, has frequently appeared in the literature. Here with $\widehat{T}_n^{\sim\varpi}$, however, it has been established that multiscale energy can be precisely represented as the product of the MWT coefficients (up to some constant multiplier). For example, the transient eddy energy extracted from $T(t)$ is simply $(\widehat{T}_n^{\sim 1})^2$ multiplied by some constant.

With MWT, the available potential energy (APE) and kinetic energy (KE) densities on window ϖ at time location n, written as A_n^{ϖ} and K_n^{ϖ}, can be obtained, and their evolution equations derived, by applying the MWT to the primitive governing equations. The reader is referred to the Appendix for details; the following is a symbolic representation (location n in the subscript is henceforth omitted for simplicity):

$$\frac{\partial A^{\varpi}}{\partial t} + \nabla \cdot \mathbf{Q}_A^{\varpi} = \Gamma_A^{\varpi} - b^{\varpi} + \mathrm{S}_A^{\varpi} + \mathrm{F}_A^{\varpi}, \tag{1}$$

$$\frac{\partial K^{\varpi}}{\partial t} + \nabla \cdot \mathbf{Q}_K^{\varpi} = \Gamma_K^{\varpi} - \nabla \cdot \mathbf{Q}_P^{\varpi} + b^{\varpi} + \mathrm{F}_K^{\varpi}, \tag{2}$$

where $\varpi = 0$ and 1 stand for the two scale windows in this study, that is, the basic flow window and the eddy window. The $\mathbf{Q}$'s with subscripts A, K and P are, respectively, fluxes of APE, KE and pressure, the Γ terms are the transfer of energy (APE or KE) to the designated scale window ϖ from other windows, b is the buoyancy conversion, and F denotes the contribution from dissipation/diffusion. Explicit expressions and detailed physical interpretations are given in the Appendix, Table A1. Note that all the terms are localized both in space and time; in other words, they are all four-dimensional field variables, distinguished notably from the classical formalisms in which localization is lost in at least one dimension of space–time in order to achieve scale decomposition. Processes localized in space and time are thus naturally embedded in Equations 1 and 2.

[1]Note that one cannot write it in terms of the filtered quantities such as $[T^{\sim 1}(t)]^2$, as multiscale energy is a concept in phase space. (Think about that in a Fourier spectrum.) Refer to the Appendix for further explanation.

Although the terms in Equations 1 and 2 have the conventional names (e.g., Orlanski and Katzfey, 1991; Chang, 1993), they are actually distinctly different from those in traditional formalisms. The most distinct terms are Γ_A^{ϖ} and Γ_K^{ϖ}, which are the processes that we are most interested in for this study. In the Appendix we will see that they both have a Lie bracket form, and possess the property of Jacobian identity, reminiscent of the Poisson bracket in Hamiltonian dynamics; they also satisfy a detailed balance relation. Most importantly, they sum to zero over scale window ϖ and location n. This conservation property, though simple to state, does not hold in previous energetic formalisms. To distinguish it from those that may have been encountered in the literature, the above transfer is termed the *canonical transfer*.

The canonical transfers (Γ_A^{ϖ} and Γ_K^{ϖ}) in Equations 1 and 2 are very important. In particular, the mean-to-eddy parts of them (written as $\Gamma_A^{0\to 1}$ and $\Gamma_K^{0\to 1}$) correspond to the two important geophysical fluid flow processes, that is, baroclinic instability and barotropic instability of the mean flow (see Liang and Robinson, 2007), although whether they are equivalent is still in dispute (e.g., Plumb, 1983; Farrell, 1984, 1985, 1989). For mnemonic reasons, in the following $\Gamma_A^{0\to 1}$ and $\Gamma_K^{0\to 1}$ may be referred to respectively as baroclinic and barotropic canonical transfers. Conversely, the eddy-to-mean parts, written as $\Gamma_A^{1\to 0}$ and $\Gamma_K^{1\to 0}$, can be used to investigate the eddy feedback processes. They correspond respectively to the baroclinic and barotropic feedback mechanisms. See Figure A1 in the Appendix for an illustration.

3.2 | Eddy tracking and compositing

The methods used in this study also include an eddy tracking and compositing technique. Because of the migration of the eddies and the inhomogeneity of the background flow, an eddy-following approach is needed to investigate the localized interaction. Here the tracking algorithm developed by Hodges (1995) is used to fulfil this task. In practical use, the maxima of the 850-hPa relative vorticity (ξ_{850}) are chosen as the indicator of the storm centre (or feature point), which forms the nodes of the storm trajectory (Hoskins and Hodges, 2002). Besides, before tracking the vorticity maxima associated with weather storms it is necessary to remove the background field, that is, the slowly varying, large spatial scale part of the field (Anderson *et al.,* 2003). Here, we use the synoptic vorticity reconstructed by the MWT as the indicator. That is to say, the eddies tracked are storms in the synoptic scale window. Following previous studies, the cyclogenesis time is defined as the first time that ξ_{850} exceeds 1×10^{-5} s^{-1}. In this study, we only select long-lived storms whose ξ_{850} remains larger than 1×10^{-5} s^{-1} for at least 4 days after their genesis. Also, only storms with a maximum ξ_{850} greater than 5×10^{-5} s^{-1} are retained for the analysis. Finally, trajectories of 2,189 cold-month (October–April) storms in the North Pacific storm-track area [20°N–70°N, 120°E–240°E]

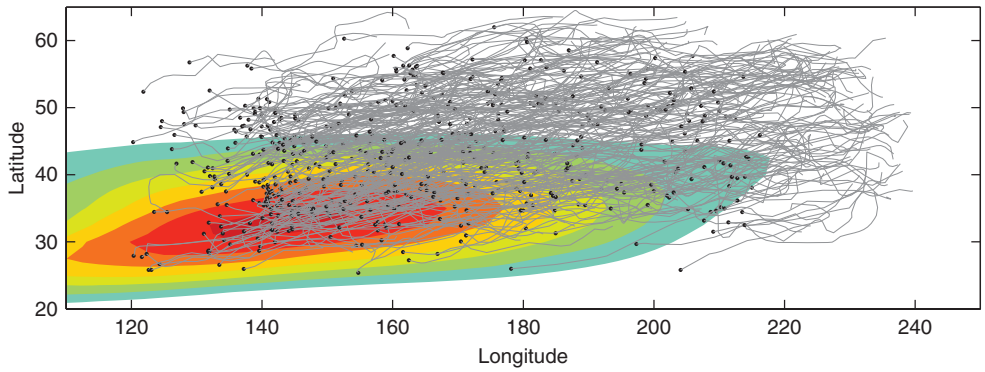

FIGURE 1 Sample of storm trajectories based on ξ_{850}. The grey lines represent trajectories, with black dots indicating their respective starting points, and the shaded area is the climatological wintertime 300-hPa zonal wind, starting from 20 m/s with an interval of 5 m/s

are obtained. A sample of the selected trajectories are displayed in Figure 1.

The cyclone trajectories obtained are used for the compositing of the spatial structures. Considering the large case-to-case variability (Sinclair and Revell, 2000), we use a compositing method with a large number of individual storms in order to get a statistical result. A detailed description of the methodology can be found in Bengtsson *et al.* (2007) for a radial sampling grid that has been modified into a rectangular sampling grid. In brief, it consists of the following procedures.

1. Select the tracks to be used. (In the present study, the storms of interest are the 2,189 long-lived strong storms.)
2. Create a rectangular grid centred on the Equator with uniform grid spacing and chosen side length (respectively 0.5 and 40° here).
3. Rotate the grid to the storm centre and rotate it to align with the direction of the storm propagation, which is determined by the displacement of the storm centre using a second-order central differencing scheme. Using the rotated composite can reduce the impact of the difference in the storm propagation direction on the composite storm structure.
4. Finally, the required field is sampled onto the rectangular grid, for each storm at each time step along the full life cycle of the storms and then averaged over the selected storms at selected stages of the life cycle. For the averaging, we need a reference time for the life cycle.

In this study, the instant of maximal intensity is chosen as $t = 0$ and the time is then measured as offset to this reference time. For example, −4 (4) stands for four time steps (or 24 hr) before (after) the storm reaches its maximal intensity. In this study, the standard deviation is used to show the case-to-case variability within the composites.

4 | MS-EVA SETUP

The analysis begins with a determination of the scale window bounds. In this study, we need two windows: a synoptic-scale window and a low-frequency background flow window. According to previous studies, these windows are set to be bounded by a period of 16 days (in MWT, the number of time steps is required to be a power of 2). We have also tried 8 days as the window bound and found that the synoptic signal cannot be completely separated from the total fields. This is essentially the same as in Deng and Mak (2006), who applied a 15-day high-pass filter in their diagnostics. Besides, Anderson *et al.* (2003) observed that band-pass filtering with a time period of 2.5–6 days (e.g., Blackmon, 1976) may have a detrimental impact on individual weather systems (see also Chang, 1993), and a 20-day high-pass filter is a good choice.

5 | COMPOSITE STRUCTURE OF THE ORIGINAL AND RECONSTRUCTED FIELDS

In this section, we briefly describe the composite structures of the original and reconstructed fields. Since the structure of each composite field changes little throughout the life of the composite storm, only the maps at the storm's maximal intensity time ($t = 0$) are presented (note that the storm strength changes significantly throughout its life; see Figures S1 and S2 in the Supporting Information). Figure 2 shows the horizontal distributions of the composite fields at 500 hPa. The side length of each subplot is 40° at the Equator (equivalent to 4,447 km). The composite system moves from the left to the right. For convenience, the along-propagation direction will be referred to as the x-direction, and the y- and z-directions are determined through the right-hand rule, with z directed upward.

5.1 | The original fields

We first look at the original fields. On the map of geopotential anomalies (ϕ) there is a trough with closed isopleths (Figure 2a). Correspondingly, a cyclonic circulation exists on the map of the horizontal wind ($\boldsymbol{v}_h$; Figure 2b). The distribution of the wind speed is quite inhomogeneous around

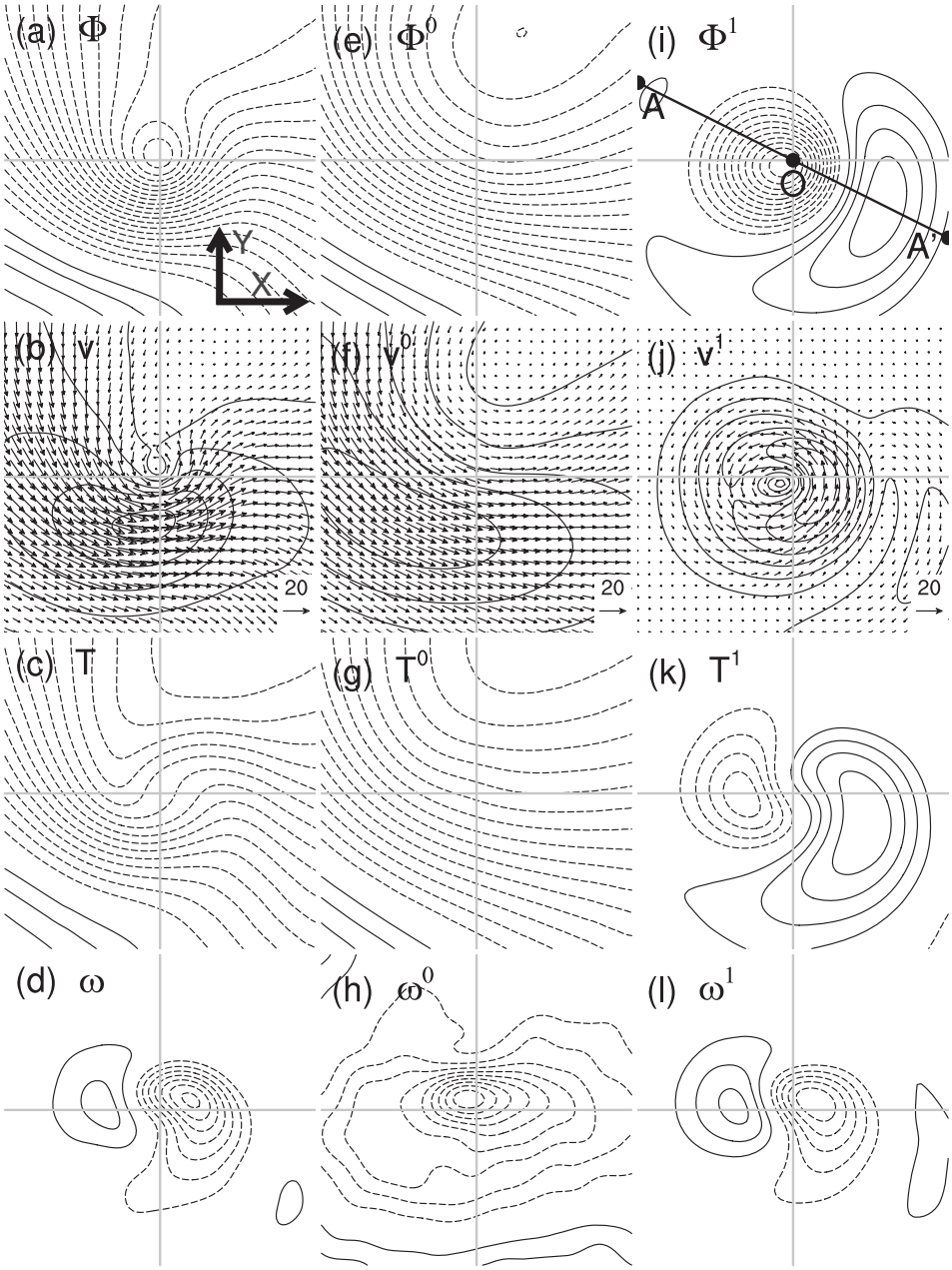

FIGURE 2 Left panels: Distributions of the 500-hPa composite original fields at the maximal intensity time ($t = 0$): (a) geopotential anomalies (contour interval 200 m^2/s^2), (b) wind vectors (m/s) and speeds (contour interval 5 m/s), (c) temperature anomalies (contour interval 1 K) and (d) vertical velocity (contour interval 0.04 Pa/s). Middle panels: The same as the left panels, but for the background fields, with contour intervals of (e) 200 m^2/s^2, (f) 3 m/s, (g) 1 K and (h) 0.004 Pa/s. Right panels: The same as the left panels, but for the synoptic fields, with contour intervals of (i) 100 m^2/s^2, (j) 2 m/s, (k) 0.5 K and (l) 0.04 Pa/s. Negative contours are indicated with dashed lines (the zero contour is omitted). The composite storm propagates eastward. Each subplot is in a 40° × 40° rectangular grid. The composites are based on the 2,185 cold-month (October–April) storms; same below (Figs. 3–9). The corresponding distributions of the standard deviation are given in Figure S3 in the Supporting Information

the storm centre, with strong winds occurring in the south part where the contours of geopotential anomalies are dense. The composite field of temperature anomalies (T) exhibits a wave-like pattern (Figure 2c), with the temperature trough and ridge located to the west and east of the storm centre, respectively. In terms of the vertical velocity (ω), it shows a dipole pattern (Figure 2d), with upward ($\omega < 0$) and downward ($\omega > 0$) motions located ahead of and behind the geopotential trough, respectively; the upward motion is much stronger than the downward motion. The features of these composite fields generally agree with those in previous studies (Field and Wood, 2007; Bengtsson *et al.,* 2009; Catto *et al.,* 2010; Dacre *et al.,* 2012).

5.2 | The multiscale window reconstructed fields

We now look at the composites of the multiscale fields reconstructed by the MWT. To our knowledge, few studies have explored the storm structure in this way. Figure 2e–h shows the composite maps of the background fields. We see

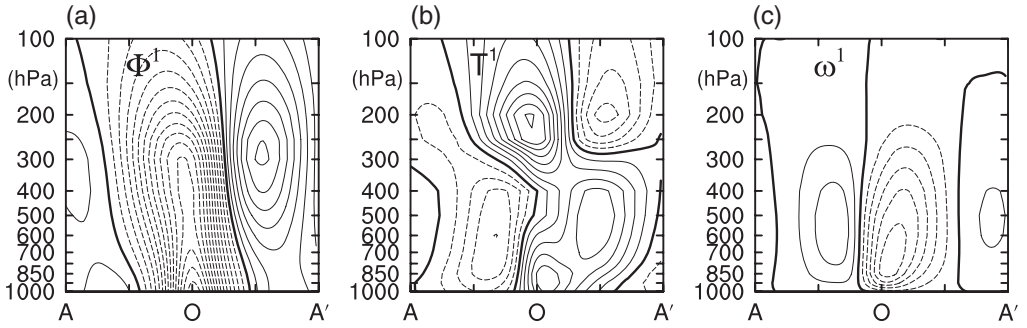

FIGURE 3 Vertical section distributions of the composites of the synoptic fields: (a) geopotential anomalies (contour interval 100 m^2/s^2), (b) temperature anomalies (contour interval 0.5 K) and (c) vertical velocity anomalies (contour interval 0.04 Pa/s). Negative contours are indicated with dashed lines and the zero contour is in bold. All these sections are taken along the line (AOA') as indicated in Figure 2i. The corresponding distributions of the standard deviation are given in Figure S4 in the Supporting Information

that the contours of geopotential anomalies ($\phi^{\sim 0}$) are generally distributed northwest–southeastward (Figure 2e), and the closed centre appearing in the original field (Figure 2a) has been removed. The background wind maximum (i.e., the jet stream) is located in the south (Figure 2f). This is why the maximum wind occurs in the southern part of the storm on the original map (Figure 2b). For temperature anomaly $T^{\sim 0}$, its distribution (Figure 2g) is similar to that of $\phi^{\sim 0}$. Regarding $\omega^{\sim 0}$, it is negative within almost the whole domain (Figure 2h), implying that the storms are generated and evolve within an environment of upward motion. The magnitude of $\omega^{\sim 0}$ is about 10% of the original field (note the difference in the contour interval between them).

Figure 2i–l shows the distributions of the composite synoptic fields, which exhibit more local features than the background fields. The composite field of the 500-hPa $\phi^{\sim 1}$ shows a low–high pair (Figure 2i). The low anomaly has compact structure and large amplitude, accompanying a strong cyclonic circulation (Figure 2j), whereas its counterpart is broad and weak. The other anomaly fields ($T^{\sim 1}$ and $\omega^{\sim 1}$) generally show a dipolar pattern (Figure 2k,l). Their distributions are configured in such a way that the moist, warm air ascends in the front part of the storm and the dry, cold air subsides in the rear part.

The vertical structure of the composite synoptic system is also examined. Figure 3 shows the distributions of the composite synoptic fields along the section AOA' as indicated in Figure 2i. This generally exhibits the structure of typical midlatitude baroclinic waves, with a zonal wavelength of ~4,000 km and a westward (eastward) tilting of the phase line of $\phi^{\sim 1}$ ($T^{\sim 1}$) with altitude (Hartmann, 1974; Lau, 1979; Lim and Wallace, 1991; Chang, 1993). Note however the strong cyclone–anticyclone asymmetry. For example, the cyclone is strongest at low levels, whereas the accompanying anticyclone achieves its maximum at upper levels with weak signals at the Earth's surface (Figure 3a).[2] For $\omega^{\sim 1}$, the upward motion in the front part is much stronger than the downward motion in the rear (Figure 3c).

[2]To the best of our knowledge, the splitting of the warm centre (at 850 hPa) ahead of the cyclone has not been observed (Figure 3b).

6 | NONLINEAR EDDY–MEAN FLOW INTERACTION

6.1 | Spatial structure of the canonical transfers

The eddy–mean flow interaction includes the canonical transfer from the mean flow to the eddies ($\Gamma_A^{0\to 1}$ and $\Gamma_K^{0\to 1}$) and for the opposite direction ($\Gamma_A^{1\to 0}$ and $\Gamma_K^{1\to 0}$). The former is a quantitative description of the mean-to-eddy transfer and the latter characterizes the eddy feedback. We first look at the spatial structure of the former.

Figure 4 shows the horizontal distributions of the vertically integrated (from 1,000 to 100 hPa) $\Gamma_A^{0\to 1}$ and $\Gamma_K^{0\to 1}$. Figure 4a shows a dipolar pattern for $\Gamma_A^{0\to 1}$, with a strong positive centre in the north of the storm and a weak negative centre in the south. This means that the background flow experiences a downscale canonical APE transfer in the north of the storm and an upscale canonical APE transfer in the southern region. The barotropic canonical transfer $\Gamma_K^{0\to 1}$ (Figure 4b) also exhibits a dipolar distribution within the storm area, with a negative region at the front and a positive one at the rear, implying upscale and downscale canonical KE transfers in the respective regions. In terms of the amplitude the negative barotropic canonical transfer centre is stronger than its positive counterpart. On the whole, the storm has a favourable configuration for APE to be transferred from the mean flow and for KE to be transferred to the mean flow, consistent with the traditional perspective (Simmons and Hoskins, 1978, 1980; Barnes and Young, 1992; Orlanski and Chang, 1993). Figure 4c shows the vertical profiles of $\Gamma_A^{0\to 1}$ and $\Gamma_K^{0\to 1}$ averaged horizontally over the storm area. We see that $\Gamma_A^{0\to 1}$ is positive almost throughout the entire troposphere. The maximum centre occurs at 400 hPa. In contrast, $\Gamma_K^{0\to 1}$ is negative throughout the whole depth, implying that the KE transfer is from the storm to the background flow. It is strong at upper levels and reaches its maximum magnitude at 250 hPa.

The spatial distributions of the eddy feedback, characterized by $\Gamma_A^{1\to 0}$ and $\Gamma_K^{1\to 0}$, are shown in Figure 5. We see that horizontally $\Gamma_A^{1\to 0}$ is negative within the entire domain (Figure 5a), implying a downscale canonical APE transfer.

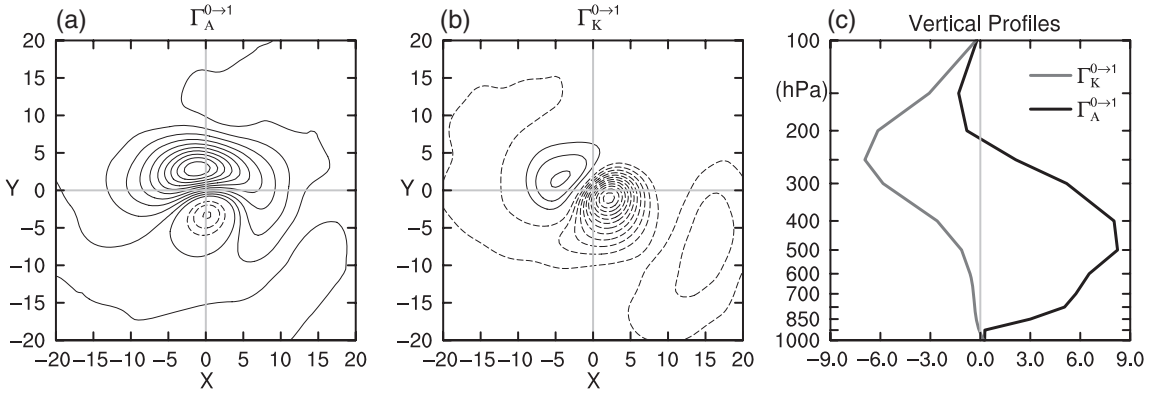

FIGURE 4 Horizontal distributions of the vertically integrated (from 1,000 hPa to 100 hPa) (a) $\Gamma_A^{0\to1}$ and (b) $\Gamma_K^{0\to1}$ at the maximal intensity time ($t=0$), with a contour interval of 2×10^{-4} m^2/s^3. (c) Vertical distributions of $\Gamma_A^{0\to1}$ and $\Gamma_K^{0\to1}$ (10^{-4} m^2/s^3) averaged over the storm area. Negative contours are indicated with dashed lines (the zero contour is omitted). The corresponding distributions of the standard deviation are given in Figure S5 in the Supporting Information

However, the transfer is inhomogeneous within the composite storm, with the strong energy transfer mainly confined to the northern area. Vertically, $\Gamma_A^{1\to0}$ is negative throughout almost the entire troposphere (Figure 5b). The peak occurs at 400 hPa and on the northern flank of the jet (also the storm centre). In short, the spatial distribution of $\Gamma_A^{1\to0}$ is similar to that of $\Gamma_A^{0\to1}$. For $\Gamma_K^{1\to0}$, it is generally positive (Figure 5c), implying an upscale KE canonical transfer. Note that this upscale transfer is significant at upper levels, especially at the jet core (Figure 5d). Figure 6 gives the vertical profiles of $\Gamma_A^{1\to0}$ and $\Gamma_A^{1\to0}$. It can be seen that their distributions are almost the same as the mean-to-eddy counterparts (Figure 4c), but with the opposite sign.

6.2 | Time evolution

The nonlinear eddy–mean flow interaction is not steady. Here, we are more interested in how the eddy feedback process evolves when there is a storm passing through. To show this for a particular storm, we first identify the central location of the storm at its maximum intensity time ($t=0$) and then sample the vertical cross section of the fields (here $\Gamma_A^{1\to0}$ and $\Gamma_K^{1\to0}$) at that location meridionally at each time step from -12 to 12 (from day -3 to day 3, correspondingly).[3] In sampling, the fields at each time step are also rotated with respect to the storm propagation direction at $t=0$. Following this method, we can get the latitude–time section of any field at a particular location as a storm approaches, passes and recedes.[4] This procedure is applied to each of the 2,189 selected storms. Finally, the obtained sections are averaged over all the samples at each time step.

Figure 7 shows the general time evolution of $\Gamma_A^{1\to0}$ and $\Gamma_K^{1\to0}$.[5] We see that as the storm passes, the downscale APE transfer is intensified within a narrow zonal band north of the storm centre, whereas elsewhere it is slightly weakened (Figure 7a). In contrast, the upscale KE transfer is intensified slightly within a narrow zonal band on the southern side, while in the north it is greatly weakened (Figure 7b). The changes of $\Gamma_A^{1\to0}$ and $\Gamma_K^{1\to0}$ begin about 3 days before the storm arrives, achieve their maxima as the storm arrives and then weaken. In the presence of the storm, $\Gamma_A^{1\to0}$ and $\Gamma_K^{1\to0}$ seem to take place complementarily in the horizontal plane: $\Gamma_K^{1\to0}$ intensifies (weakens) whenever $\Gamma_A^{1\to0}$ substantially weakens (intensifies).

The most interesting finding in this section is the spatial asymmetry of the eddy–mean flow interaction: the downscale canonical APE transfer process mainly happens in the northern part of the storm (also on the northern flank of the jet stream) and in middle levels, whereas the upscale canonical KE transfer mainly occurs in the south, overlaid with the jet core. The former acts to destroy the background baroclinicity, whereas the latter acts to accelerate the jet and thus enhance the baroclinicity. These competing effects essentially determine the final state of the jet stream after the storm passes. We will elaborate on this in the following section.

7 | RESPONSE OF THE BACKGROUND FLOW AND BAROCLINICITY

In this study, we focus on the responses of the background wind and baroclinicity. Figure 8 shows the composite sections of the background wind (left panels). We see that as the storm passes, the wind decreases in the north but increases in the south, showing an anomalous dipolar pattern (Figure 8a). Moreover, the increase in the south is stronger than the decrease in the north. Since the jet core is located in the south of the storm (cf. Figure 3), this tends to strengthen and narrow the jet (by two latitudes).[6] Figure 8c,d shows

[3]Here we choose a duration of 6 days, considering that the mean life cycle of the 2,189 storms lasts 5.37 (±1.45) days.
[4]Here we switch to the Eulerian approach in order to obtain the spatio-temporal distribution of the interaction and, particularly, the background flow response (see below).
[5]In this figure we want to see the change in energy transfer at the site of observation as a storm approaches, passes and recedes, so we choose an earlier day (i.e., day -3) rather than day 0 when the storm is passing.
[6]This estimation is based on the half jet-width, which is measured by the distance between the latitude of maximum wind and the northward latitude at which the wind reaches half of its peak.

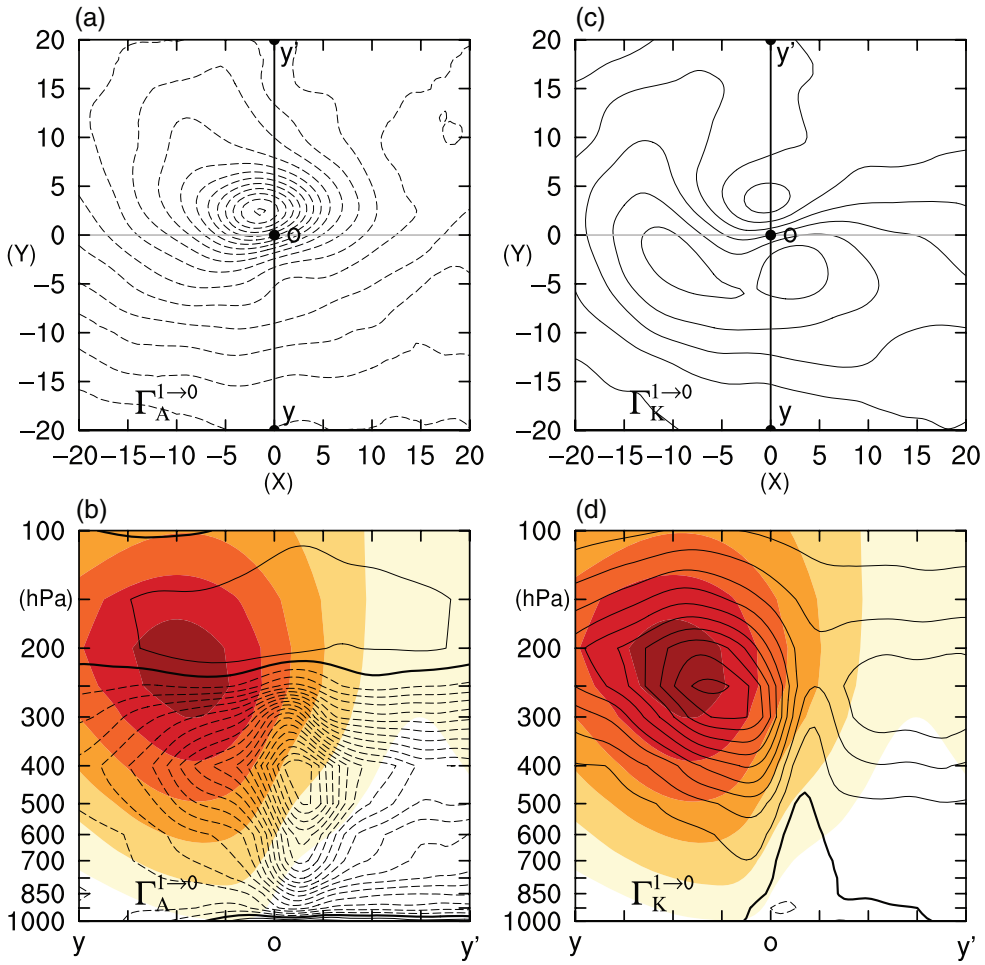

FIGURE 5 Spatial distributions of $\Gamma_A^{1\to0}$ and $\Gamma_K^{1\to0}$ at the maximal intensity time ($t=0$): the vertically averaged (a) $\Gamma_A^{1\to0}$ and (c) $\Gamma_K^{1\to0}$ and the sectional distributions of (b) $\Gamma_A^{1\to0}$ and (d) $\Gamma_K^{1\to0}$ along the line yoy' as indicated in (a) and (c). Negative contours are indicated with dashed lines and the zero contour is in bold. The contour interval is 0.5×10^{-4} m^2/s^3. In (b) and (d), the background wind speed $|\overline{v}^{0}|$ is overlaid (shaded; contour interval 4 m/s). The corresponding distributions of the standard deviation are given in Figure S6 in the Supporting Information

the composite pressure–time sections of the background wind along the latitudes of 10° and −10°, respectively. It can be seen that either in the north or in the south, the response of the background wind is more significant in the upper troposphere (Figure 8b,c). Temporally, the background wind begins to change about 3 days before the storm's arrival and responds strongly as the storm arrives. A closer observation reveals that the largest change occurs at $t=2d$ instead of $t=0$ (see also the energy transfers in Figure 7). This may be due to the consecutive influence of secondary cyclones formed along the trailing cold front of the reference one (e.g., Papritz and Schemm, 2013). Overall, the jet does not show any obvious meridional shift. This is consistent with the argument of Vallis and Gerber (2008), that if the storm is generated on the flank of the jet the storm will act to maintain the jet's latitude. For the background wind response at any instant (e.g., $t=0$), the meridional structure is similar to that obtained by Chang (2001b) using wave packet regression.

The latitude–time section of the baroclinicity, measured by $fN^{-1}|\partial\overline{v}/\partial z|$ (where N is the static stability and other symbols are conventional), is also shown in Figure 8 (right panels). We see that, as the storm passes, the baroclinicity weakens in the north but strengthens in the south (Figure 8d). Vertically, the largest northern weakening happens in the lower troposphere (Figure 8e), while the strongest southern strengthening occurs at middle levels (Figure 8f).

There is a discrepancy between the evolution of the energy transfers and that of the background flow. Figure 7 suggests that the downscale transfer north of the cyclone is much stronger than the upscale transfer south of the cyclone, while Figure 8 shows that the jet/baroclinicity decrease north of the cyclone is somewhat smaller than the one south of the cyclone. How does this discrepancy occur? In fact, the energy transfer is not the only factor that can cause a change in the background field. In addition to the nonlinear interaction process, many other energy processes (e.g., energy flux convergences) are also involved, and these can redistribute the energy in horizontal space (Papritz and Schemm, 2013; Rivière *et al.,* 2015). Figure 9 shows the mean distribution of the horizontal KE flux convergence along the meridional direction. It can be seen that the convergence is strong on the southern side of the storm centre and peaks near the jet centre. Moreover, the convergence is mainly due to the zonal component of the KE flux (Figure 9b). This indicates that, apart

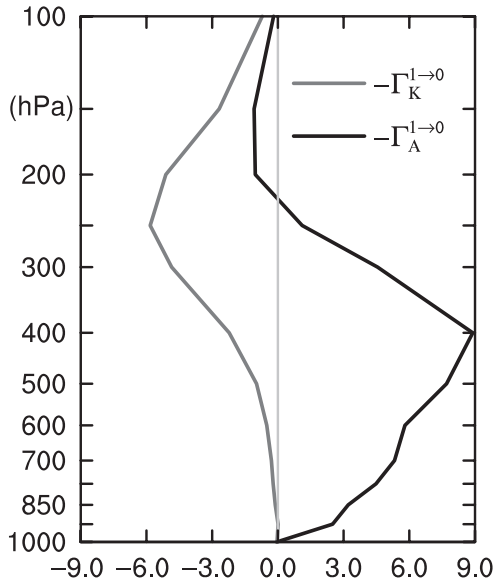

FIGURE 6 The vertical distributions of $-\Gamma_A^{1\to0}$ and $-\Gamma_K^{1\to0}$ (10^{-4} m^2/s^3) averaged over the storm area

from the energy transfer, nonlocal processes also play a role in the enhancement of the background flow in the southern part of the storm.

8 | DISCUSSION

In the above we have discussed the average results of all the 2,189 storms, and overall the composite storm is located on the northern side of the maximum background wind speed (refer to Figures 2, 5, and 8). If we have a closer look at these storms, however, there are in fact four types of relative locations that can be classified.

In order to determine the relative location of a storm, we sample the 300-hPa zonal wind in equal distance along the meridian passing through the storm centre. We take the centre as the starting point (0°) and sample the wind speed once every 2.5° to the south and to the north, respectively. The sampling range is from −20° (south) to 20° (north). Based on the resulting meridional profile of the background zonal wind, the relative location is then determined. We first calculate the average meridional gradient of zonal wind north and south of the storm centre, which here is simply represented by the difference $\Delta = \overline{u_{i+1}} - \overline{u_i}$ (the overbar stands for meridional average). For convenience, the average gradients on the southern side and the northern side are referred to as Δ_S and Δ_N, respectively. If $\Delta_S < 0$ and $\Delta_N < 0$, it means that the storm centre is located on the northern side of the jet, and we call this type of configuration Type 1; if $\Delta_S > 0$ and $\Delta_N > 0$, the storm centre is located on the southern side of the jet, and we call this configuration Type 2; if $\Delta_S > 0$ and $\Delta_N < 0$, the storm is at the centre of the jet, and the configuration is classified as Type 3; if $\Delta_S < 0$ and $\Delta_N > 0$, it means that there are two jets, and the storm lies in between – we call this configuration Type 4.

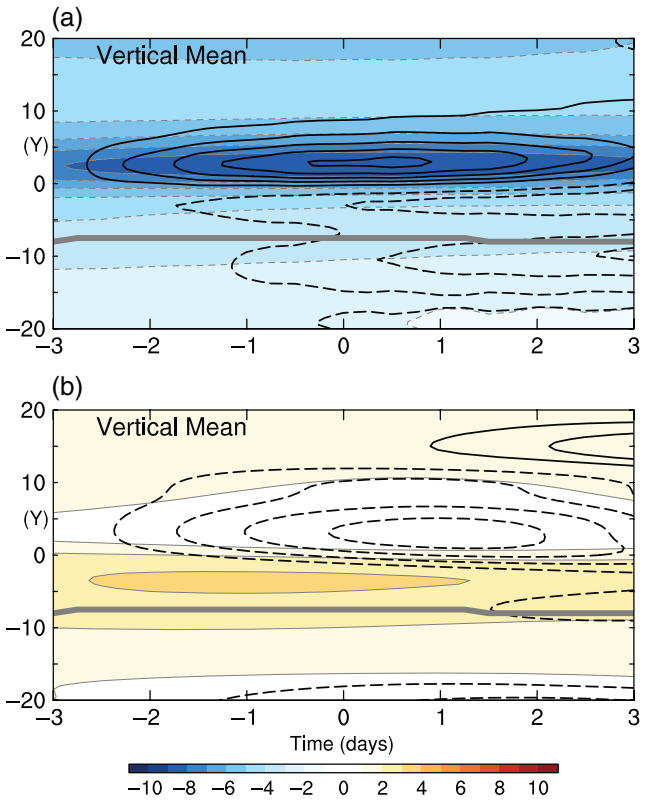

FIGURE 7 Vertically averaged latitude–time sections of the composite $\Gamma_A^{1\to0}$ (a; 10^{-4} m^2/s^3) and $\Gamma_K^{1\to0}$ (b; 10^{-4} m^2/s^3). The contours show the changes in magnitude relative to the initial state (at day −3), which are calculated as $A' = |A| - |A_*|$, with A the original field and A_* the field at day −3. Negative contours are indicated with dashed lines (the zero contour is omitted). The contour interval is 0.2×10^{-4} m^{-2}/s^3. The thick grey curve in (a) and (b) denotes the latitude where the 300-hPa background wind is maximized (i.e., the jet axis). The corresponding distributions of the standard deviation are given in Figure S7 in the Supporting Information

By the above classification it is found that there are 909 Type-1, 93 Type-2, 881 Type-3 and 299 Type-4 configurations, plus 7 cases belonging to no type. The mean meridional profiles of the background zonal wind corresponding to these four configuration types are shown in Figure 10. It can be seen that if only the configuration between the storm and the major jet is considered, the Type-4 case is similar to the Type-1 case, that is, the configuration with storms located on the northern side of the major jet. The result is that Type-1 and Type-4 storms together account for 55.2% of the total 2,189 storms, consistent with the previous observation that the storm track is generally located on the poleward flank of the jet (e.g., Blackmon *et al.,* 1977; Chang *et al.,* 2002). On the other hand, the Type-3 storms are not located exactly at the centre of the jet, but northward of it by 2.5°. Despite being in a minority, 93 storms appear on the southern side of the jet. One may wonder whether these four kinds of storms have different interaction scenarios from each other. In the following, we discuss these four storm types separately and compare and contrast them.

Figure 11 shows the distribution of the composite 500-hPa geopotential anomalies for the four storm types. As expected, the distributions of the Type-1 and Type-4 storms are similar

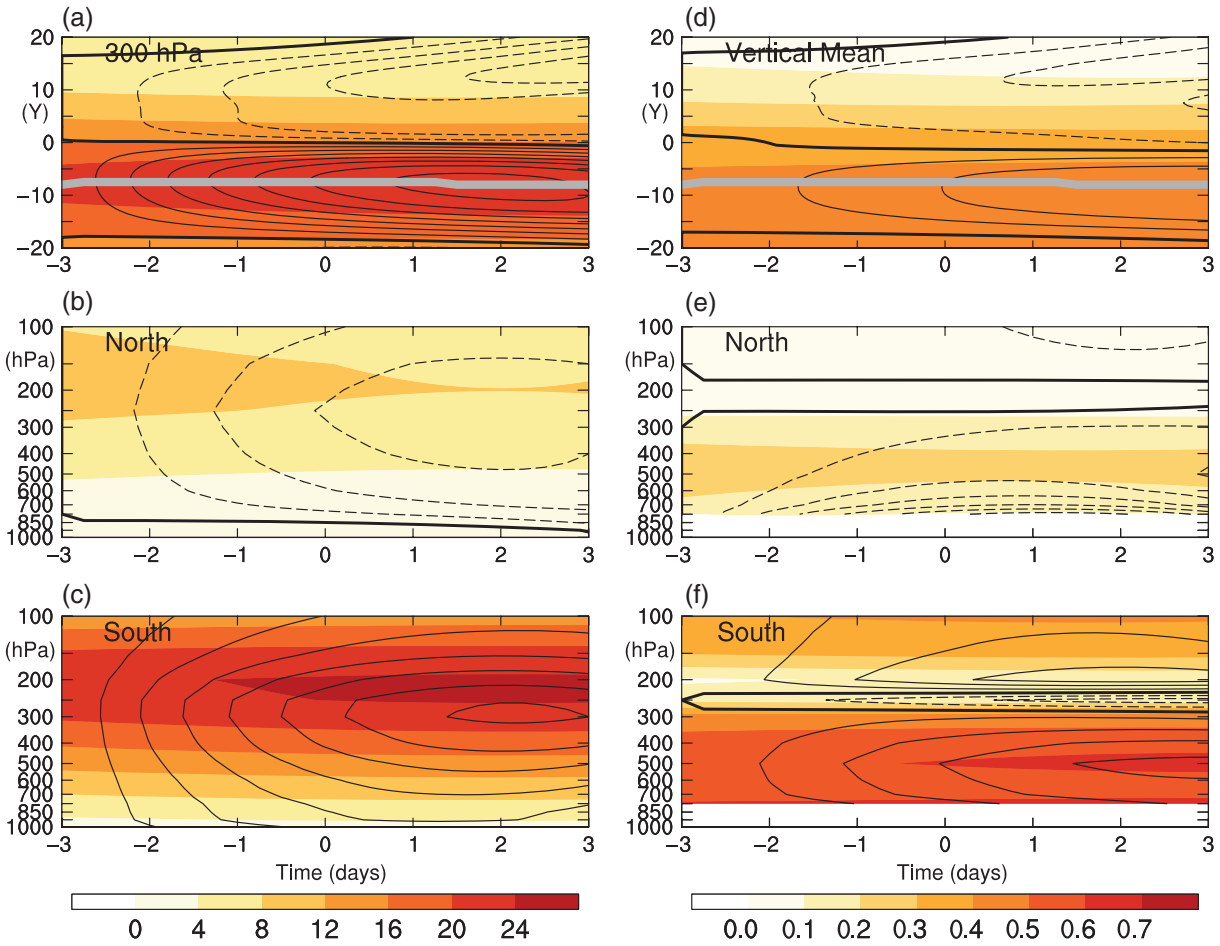

FIGURE 8 Left panels: The same as Figure 7, but for the background wind speed (shaded, m/s) and its anomaly (contoured, with an interval of 0.25 m/s); (a) shows the latitude–time section at 300 hPa; (b) and (c) show the pressure–time sections along the latitudes of 10° and −10°, respectively. Negative contours are indicated with dashed lines and the zero contour is in bold. The thick grey curve in (a) and (d) denotes the latitude of the maximum of the 300-hPa background wind. Right panels: The same as the left panels, but for baroclinicity, that is, the Eady growth rate (shaded; in day^{-1}) and its anomaly (contoured, with an interval of 0.01 day^{-1}). The corresponding distributions of the standard deviation are given in Figure S8 in the Supporting Information

since both of them are located on the northern flank of the jet. Besides, their distributions (Figure 11a–c,j–l) are similar to the general results as shown in Figure 2a,e,i, with a wide trough in the background field (Figure 11b,k) and a dipole in the synoptic field (Figure 11c,l). This is easy to understand because these two types together account for the largest proportion of the total storms. Although the Type-3 storm is located near the jet centre, the distribution of its geopotential anomalies (Figure 11g–i) is still similar to those of Type 1 and Type 4. The obvious difference lies with the Type-2 storm. There is a distinct anticyclonic circulation on the southern side of the storm in the original field (Figure 11d), which is not seen for the other three types. In addition, it can be found that the propagation direction of the Type-2 storm is basically parallel to the isolines of the background geopotential (Figure 11e), whereas that of the other three types intersects the isolines and points to the left side.

The horizontal distributions of the vertically integrated canonical transfers $\Gamma_A^{0\to1}$ and $\Gamma_K^{0\to1}$ are given in Figure 12.[7] It can be seen that the Type-1 (Figure 12a,b), Type-3 (Figure 12g,h) and Type-4 (Figure 12j,k) storms generally bear the same structure, similar to the general results as shown in Figure 4. For instance, $\Gamma_A^{0\to1}$ shows a dipolar pattern, with a strong positive centre in the north of the storm and a weak negative centre in the south. $\Gamma_K^{0\to1}$ also exhibits a dipolar distribution within the storm area, with a negative centre at the front and a positive one in the rear (note that the positive $\Gamma_K^{0\to1}$ centre in the Type-4 storm is not obvious). In contrast, the Type-2 storm is quite different. Horizontally, $\Gamma_A^{0\to1}$ is mainly distributed in the northeast corner with small values (Figure 12d), and there is no dipole pattern as observed in the other three types. $\Gamma_K^{0\to1}$ does not show the dipolar structure

[7] Although there appears to be a significant difference between the horizontal distributions of the Type-2 (Figure 12e) and Type-3 (Figure 12h) KE transfers, the corresponding vertical profiles (Figure 12f,i) are almost identical. We remark that this is only an optical illusion. We see that although the upscale KE transfer centre of Type 2 (Figure 12e) is weaker than that of Type 3 (Figure 12h), the former has a larger scope than the latter. Besides, Type 3 has a strong downscale KE transfer in the northwest part (Figure 12 h), which is lacking in Type 2 (Figure 12e). On the horizontal average, therefore, it is not surprising to observe almost identical vertical profiles. A similar argument applies to the APE transfer (i.e., Figure 12g,i,j,l). Although the downscale APE transfer is much stronger in Type 3 than in Type 4, in Type 3 it is confined to a more limited area. As a result, the horizontal mean of Type 3 is only slightly larger than that of Type 4.

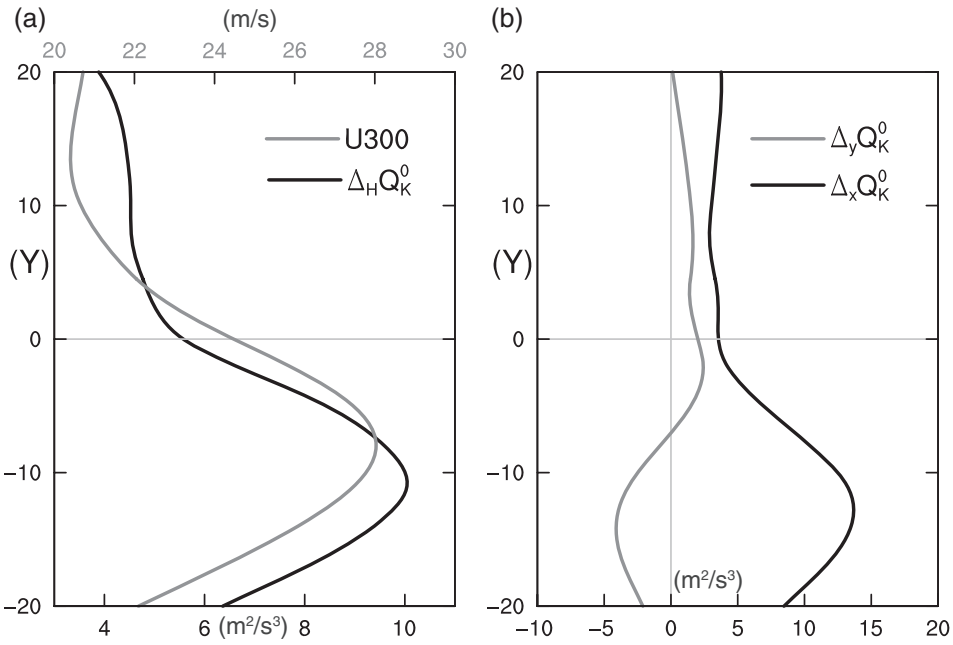

FIGURE 9 (a) Mean distributions of the horizontal kinetic energy flux convergence (in black; 10^{-4} m^2/s^3) and the 300-hPa wind speed (in grey; m/s) versus *y*; (b) the same as (a), but for the *x*- and *y*-components of the kinetic energy flux convergence

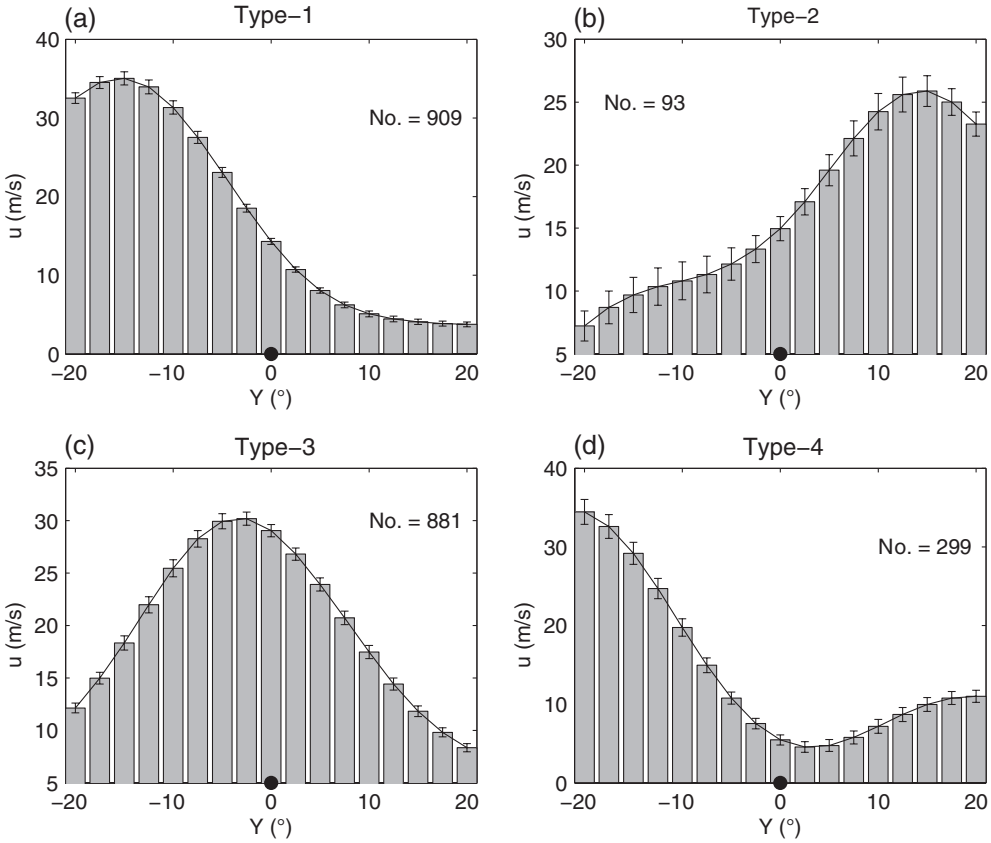

FIGURE 10 The four types of zonal wind profiles. (a) Type-1: The storm is on the northern side of the jet; (b) Type-2: The storm is on the southern side of the jet; (c) Type-3: The storm is at the jet centre; and (d) Type-4: The storm is located between two jets. The black dots indicate the meridional location of the storm centre for each type. The error bars represent the uncertainties of the mean at the 5% significance level

either (Figure 12e); it is negative throughout the domain, with two minima around the storm centre.

Also presented in Figure 12 are the average vertical distributions of $\Gamma_A^{0\to1}$ and $\Gamma_K^{0\to1}$. The Type-1 (Figure 12c), Type-3 (Figure 12i) and Type-4 (Figure 12l) storms have the largest amplitude of $\Gamma_A^{0\to1}$ ($\Gamma_K^{0\to1}$) at middle (high) levels, similar to the general results previously revealed in Figure 4c. For the Type-2 storm, its $\Gamma_K^{0\to1}$ profile is also similar, but its

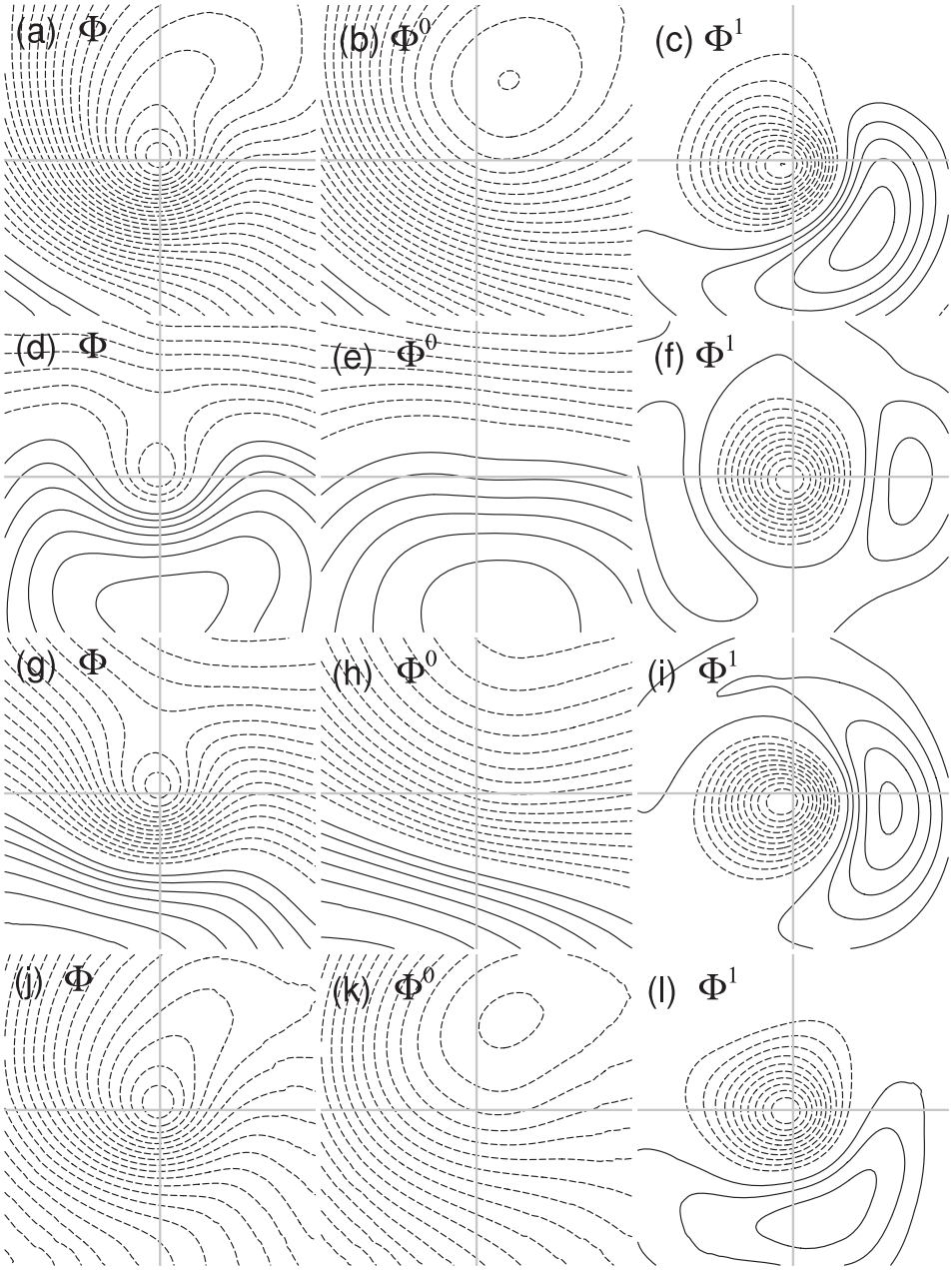

FIGURE 11 The same as Figure 2a,e,i, but for the Type-1 (a–c), Type-2 (d–f), Type-3 (g–i) and Type-4 (j–l) storms, respectively. The corresponding distributions of the standard deviations are displayed in Figure S9 in the Supporting Information

TABLE 1 The average $\Gamma_A^{0\to1}$ and $\Gamma_K^{0\to1}$ for the four storm types and the corresponding absolute ratio $|\Gamma_A^{0\to1}/\Gamma_K^{0\to1}|$

	Type-1	Type-2	Type-3	Type-4
$\Gamma_A^{0\to1}$ (10^{-4} m^2/s^3)	5.3	1.5	3.7	3.5
$\Gamma_K^{0\to1}$ (10^{-4} m^2/s^3)	−1.9	−2.1	−2.1	−1.7
$\lvert\Gamma_A^{0\to1}/\Gamma_K^{0\to1}\rvert$	2.7	0.7	1.8	2.0

$\Gamma_A^{0\to1}$ profile is quite different. Although it is still positive throughout most of the troposphere, it is quite weak; refer to Table 1 for a quantitative comparison.

Figure 13 gives the distributions of $\Gamma_A^{1\to0}$ and $\Gamma_K^{1\to0}$ over the meridional section through the storm centre. For $\Gamma_A^{1\to0}$, there is always an active centre on the northern side of the Type-1 (Figure 13a), Type-3 (Figure 13g) and Type-4 (Figure 13j) storms (as well as the jets), which is lacking in the Type-2 storm (Figure 13d). For $\Gamma_K^{1\to0}$, its centre generally coincides with the jet stream. In addition, $\Gamma_K^{1\to0}$ seems to be enhanced in the southern part of the storm. For instance, the $\Gamma_K^{1\to0}$ maximum always occurs there, although the jet is sometimes located in the north (see Figure 13e). Vertically, the distributions of $\Gamma_A^{1\to0}$ and $\Gamma_K^{1\to0}$ (Figure 13c,f,i,l) are basically the same as the mean-to-eddy counterparts (Figure 12c,f,i,l), but with the opposite sign.

An interesting result of the above analysis is the difference in the downscale canonical transfers of APE (see Table 1 and Figure 13). One can see that, although the Type-1 storm is located far from the jet, its downscale APE transfer is stronger than that of the Type-3 storm, which is near the jet core.

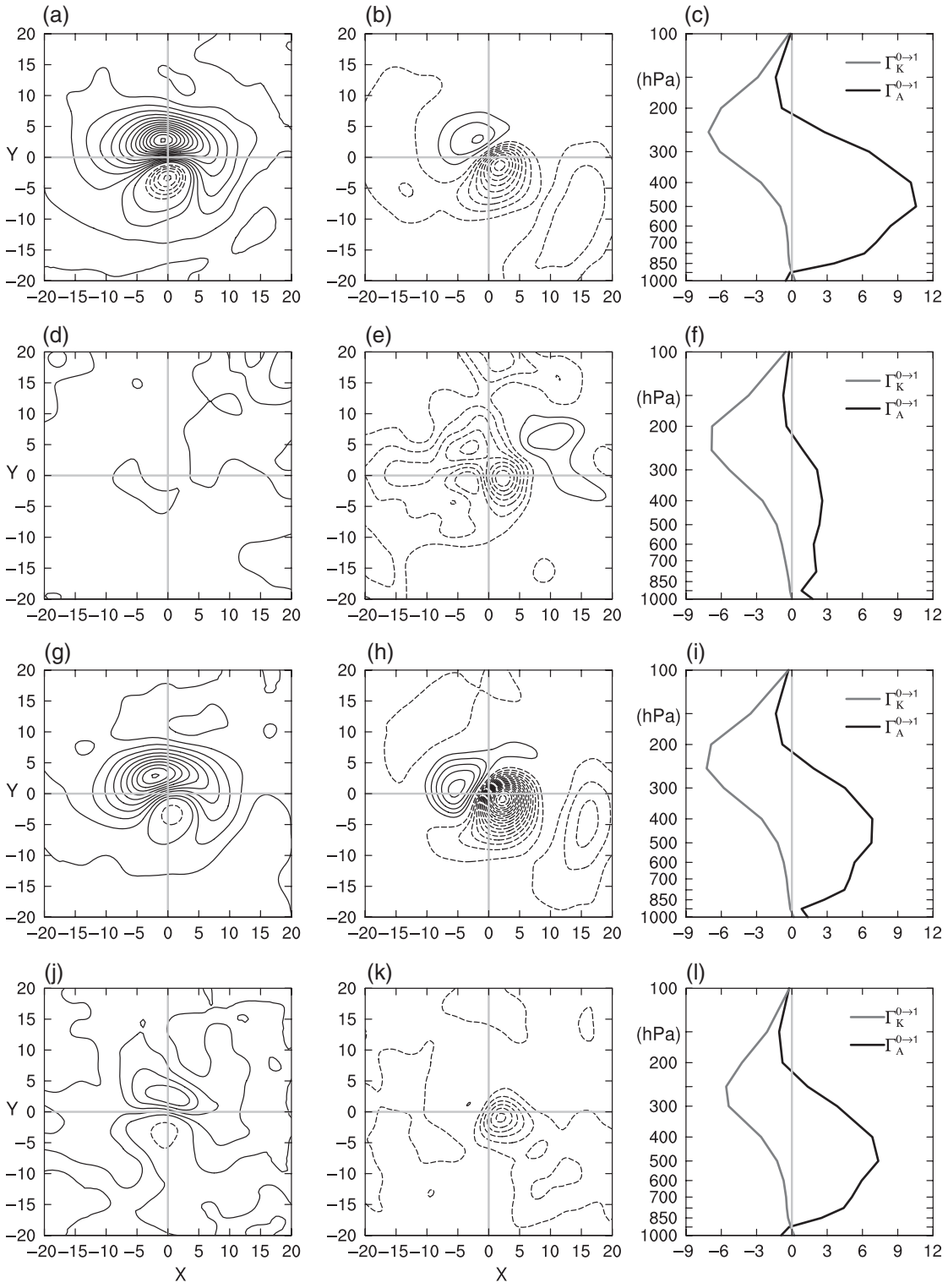

FIGURE 12 The same as Figure 4, but for the Type-1 (a–c), Type-2 (d–f), Type-3 (g–i) and Type-4 (j–l) storms, respectively. Left panels: $\Gamma_A^{0\to1}$; middle panels: $\Gamma_K^{0\to1}$; right panels: Vertical distributions of $\Gamma_A^{0\to1}$ and $\Gamma_K^{0\to1}$. The corresponding distributions of the standard deviations are given in Figure S10 in the Supporting Information

This result seems to contradict the traditional linear baroclinic instability theory (Eady, 1949; Lindzen and Farrell, 1980), which predicts a stronger baroclinic instability given a relatively stronger zonal wind. Indeed, this kind of counter-intuitive phenomenon is not unusual; similar cases have long been discovered. One example is the midwinter minimum (MWM) of the Pacific storm-track strength. It has been found that the Pacific storm track is weaker in midwinter (when the Pacific jet stream is strongest) than in late autumn and early spring, in sharp contrast to what one would expect (Nakamura, 1992). Another example is the inverse relationship between the wintertime Pacific storm-track intensity and the jet-core strength. Previous studies have shown that in boreal winters when the Pacific jet is extremely strong, the Pacific

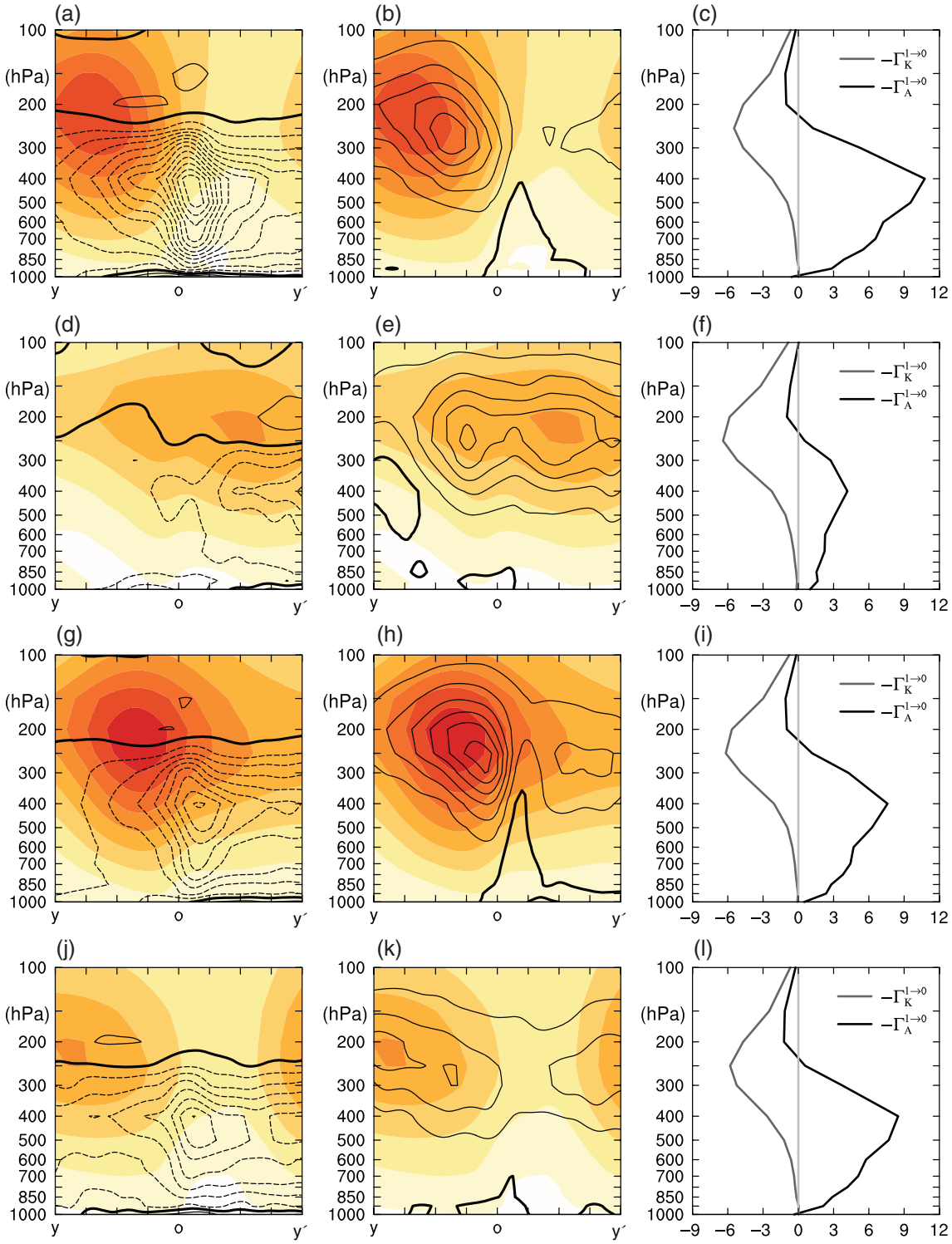

FIGURE 13 The same as Figures 5 and 6, but for the Type-1 (a–c), Type-2 (d–f), Type-3 (g–i) and Type-4 (j–l) storms, respectively. Left panels: $\Gamma_A^{1\to0}$; middle panels: $\Gamma_K^{1\to0}$; right panels: Vertical distributions of $\Gamma_A^{0\to1}$ and $\Gamma_K^{0\to1}$. The corresponding distributions of the standard deviations are given in Figure S11 in the Supporting Information

storm track is, however, unexpectedly weak (e.g., Chang, 2001a, 2001b; Penny *et al.,* 2013; Zhao and Liang, 2018). Recently, a similar situation has also been found to exist in the East Asia region. Zhao *et al.* (2018) observed that in East Asia the southern storms (south of ~41°N) mostly occur at the jet core, whereas the northern storms (north of ~41°N) are generated to the far north of the jet core; however, the downscale APE transfer in the former is found to be weaker than that of the latter (refer to figs. 6 and 9 in Zhao *et al.* [2018]). So far, there has been no agreement on what determines these counterintuitive phenomena. One possible reason is that the canonical APE transfer is likely to be more closely associated with the sea surface temperature front at midlatitudes than with the jet stream to the south (e.g., Brayshaw *et al.,* 2008), but it will require many more studies before a conclusion can be drawn on this.

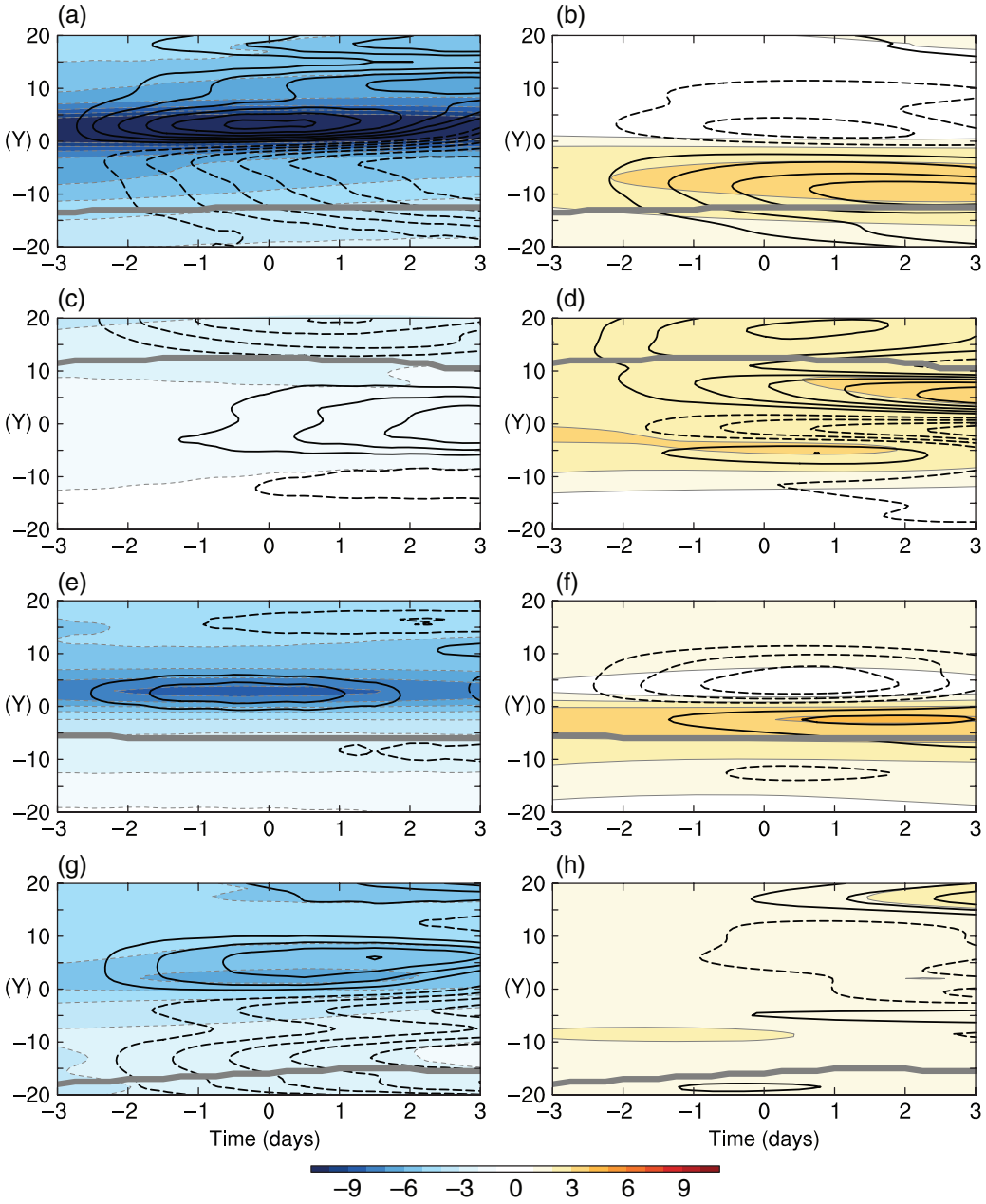

FIGURE 14 The same as Figure 7a,b, but for the Type-1 (a, b), Type-2 (c, d), Type-3 (e, f) and Type-4 (g, h) storms. Left panels: $\Gamma_A^{1\to0}$; right panels: $\Gamma_K^{1\to0}$. The thick grey curve denotes the latitude of the maximum of the 300-hPa background wind. The corresponding distributions of the standard deviations are given in Figure S12 in the Supporting Information

The time evolution of the vertically averaged $\Gamma_A^{1\to0}$ and $\Gamma_K^{1\to0}$ is given in Figure 14. Generally, the evolutions of Type 1, Type 3 and Type 4 are similar, with $\Gamma_A^{1\to0}$ ($\Gamma_K^{1\to0}$) strengthened in the north (south) of the storm and weakened in the south (north). In contrast, Type 2 is different. Its $\Gamma_A^{1\to0}$ is strengthened near the storm centre and is weakened in the south and north (Figure 14c), whereas $\Gamma_K^{1\to0}$ changes in the opposite direction (Figure 14d).

To show the response of the background wind, displayed in Figure 15 is the time evolution of the background wind speed at the lower and upper tropospheric levels. Under the influence of the storm (of any type), the background wind speed is weakened in the north of the storm and strengthened in the south, showing an anomalous dipolar distribution. Besides, the background wind response basically shows an equivalent barotropic structure in the vertical direction, and the response is most prominent at upper levels. It is worth noting that the Type-1, Type-3 and Type-4 storms are located near and to the north of the jet centre, thus accelerating the jet, whereas the Type-2 storm is located on the south side of the jet centre, weakening the jet. In addition, the wind response to the Type-2 storm is more complex than for the other three types (see Figure 15c,d). In general, the response of the background wind speed is consistent with that of the canonical transfers, except for Type 2, implying that other processes may also play a role for this storm type (refer to Section 7).

To summarize, all the four storm types basically exhibit a north–south asymmetry in the interaction with the

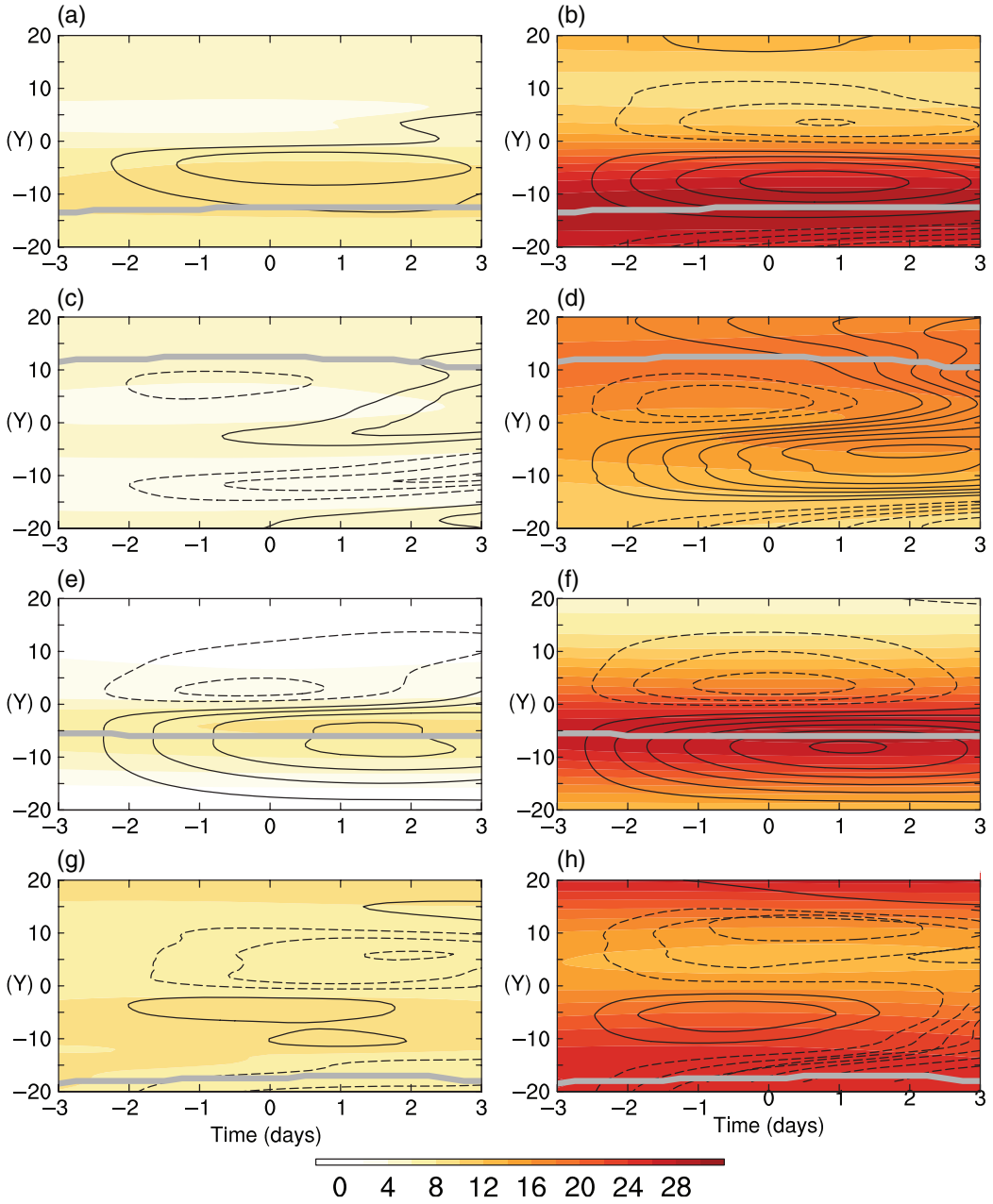

FIGURE 15 The same as Figure 8a, but for the Type-1 (a, b), Type-2 (c, d), Type-3 (e, f) and Type-4 (g, h) storms. Left panels: 850 hPa; right panels: 300 hPa. The thick grey curve denotes the latitude of the maximum of the 300-hPa background wind. The corresponding distributions of the standard deviations are given in Figure S13 in the Supporting Information

background flow, especially when the storm appears near or to the north of the jet centre. When the storm lies to the south of the jet, the baroclinic canonical transfer turns out to be weak and its overall transfer is also weakened, quite differently from the other three types. The response of the background wind field to the four storm types generally exhibits a north–south oriented dipolar distribution, with a positive anomaly in the south and a negative anomaly in the north. The Type-1, Type-3 and Type-4 storms strengthen the jet stream,[8] whereas the Type-2 storm weakens it.

In short, the interaction and background wind response for the Type-1, Type-3 and Type-4 storms are essentially similar to what has been obtained previously with all the storms considered together. The discrepancy is with the Type-2 storm. However, it should be noted here that the sample for this type is too small (with only 93 members). Its contribution is thus relatively limited and, besides, the reliability of the result also needs to be further verified.

9 | CONCLUSIONS

Using a recently developed methodology, namely the multiscale window tansform (MWT) and the MWT-based localized multiscale energetics analysis and vorticity analysis

[8]For the Type-4 storm, the strengthening of the background wind at upper level happens on the northern flank of the jet.

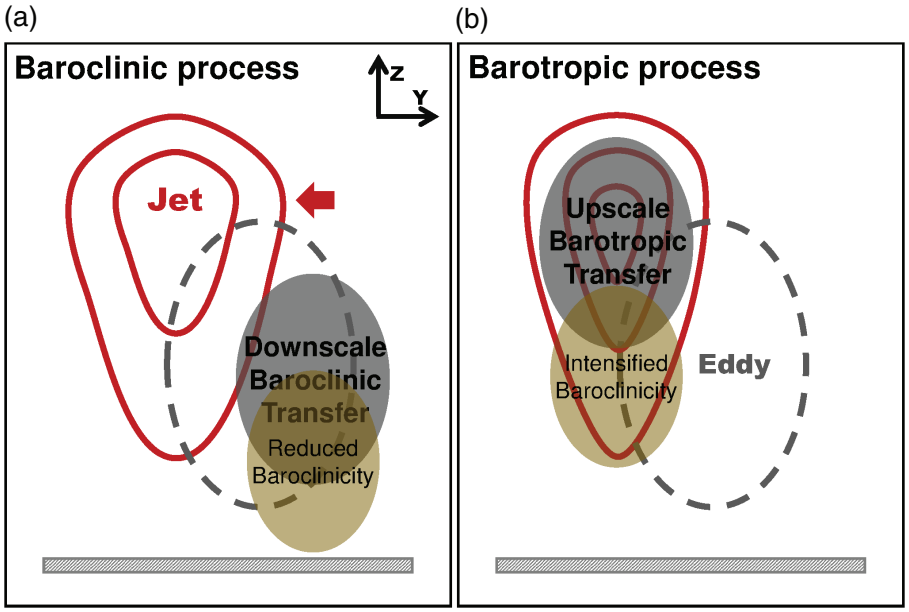

FIGURE 16 Schematic of the typical eddy feedback in the North Pacific storm track: (a) the bacroclinic processes, and (b) the barotropic processes. Solid and dashed contours denote the jet and the synoptic eddy, respectively. The dark shaded areas represent the canonical energy transfer centres, and the light shaded areas are those with a change in baroclinicity. The arrow in (a) indicates the shrinking of the jet, and the plus sign in (b) indicates the jet acceleration

(MS-EVA), as well as an eddy tracking and compositing technique, this study investigates the general structure of the nonlinear interaction between the individual synoptic eddies and the jet stream over the North Pacific storm track, based on the ERA-40 reanalysis data from ECWMF.

It is found that in the North Pacific storm track more than 50% of the storms (Type 1 and Type 4) happen on the northern flank of the jet, about 40% are near the jet centre, and very few occur south of the jet (less than 5%). For the latter, the baroclinic canonical transfer is rather weak. For the former types of storms (near or to the north of the jet centre), their interaction with the background flow is asymmetric in space. Specifically, the storms in the north experience a strong downscale canonical transfer of APE, which weakens the baroclinicity and the background wind (Figure 16a, baroclinic process), while in the south a strong upscale canonical transfer of KE happens at the jet core which accelerates the jet and enhances the baroclinicity (Figure 16b, barotropic process). The resultant effect is that the jet strengthens but narrows, resulting in an anomalous dipolar pattern in the background wind and baroclinicity field. (Note that the response of the jet may also be partially due to other processes such as large-scale energy fluxes.) On average, the local interaction begins about 3 days before a storm arrives at the site of observation, achieves its maximum as the storm arrives and then weakens.

In this study, the eddy–mean flow interaction has been investigated within the whole north Pacific storm track throughout the entirety of the cold season (October–April) without considering the spatio-temporal variability, which is worth further investigation. As we know, the strength and latitudinal location of the jet change remarkably with time throughout the year (e.g., the jet is strong and located more equatorward in winter while it is weak and located more poleward in summer). Changes in the jet's strength and latitudinal location may lead to different eddy–mean flow interactions (Nakamura, 1992; Chang, 2001a; Harnik and Chang, 2004; Penny *et al.,* 2013; Zhao and Liang, 2018). Besides, the eddy–mean flow interaction in the Atlantic sector may have a different scenario, which is certainly worth investigating. Previous studies have shown that the Pacific jet is more subtropical (Lee and Kim, 2003), whereas the Atlantic jet is largely eddy driven (Woollings *et al.,* 2010). Both the Atlantic jet and the storm track are more southwest–northeast oriented than their counterparts over the Pacific. Moreover, it has been shown (Woollings *et al.,* 2010; Franzke *et al.,* 2011; Novak *et al.,* 2015) that the wintertime North Atlantic jet exhibits significant latitudinal variability, with evidence of three preferred latitudinal locations: south, middle and north. The corresponding storm-track characteristics may be quite different, suggesting a potentially more complex eddy–mean flow interaction pattern in the Atlantic sector. We will explore these problems as the next step in our studies.

ACKNOWLEDGEMENTS

The suggestions of two anonymous reviewers are sincerely appreciated. This study was partially supported by the National Program on Global Change and Air-Sea Interaction (GASI-IPOVAI-06), by the Jiangsu Provincial Government through the 2015 Jiangsu Program for Innovation Research and Entrepreneurship Groups and the Jiangsu Chair Professorship to XSL, and by the National Natural Science Foundation of China under grant nos. 41276032 and 41705024. KIH was partly funded by NERC National Centre for Atmospheric Science (NCAS).

ORCID

Yuan-Bing Zhao https://orcid.org/0000-0002-7880-7045
X. San Liang https://orcid.org/0000-0001-8472-3211

REFERENCES

Anderson, D., Hodges, K.I. and Hoskins, B.J. (2003) Sensitivity of feature-based analysis methods of storm tracks to the form of background field removal. *Monthly Weather Review*, 131, 565–573. https://doi.org/10.1175/1520-0493(2003)131<0565:SOFBAM>2.0.CO;2.

Andrews, D.G. and McIntyre, M.E. (1978) Generalized Eliassen–Palm and Charney–Drazin theorems for waves on axisymmetric mean flows in compressible atmospheres. *Journal of the Atmospheric Sciences*, 35, 175–185. https://doi.org/10.1175/1520-0469(1978)035<0175:GEPACD>2.0.CO;2.

Barnes, E.A. and Hartmann, D.L. (2011) Rossby wave scales, propagation, and the variability of eddy-driven jets. *Journal of the Atmospheric Sciences*, 68, 2893–2908. https://doi.org/10.1175/JAS-D-11-039.1.

Barnes, J.R. and Young, R.E. (1992) Nonlinear baroclinic instability on the sphere: multiple life cycles with surface drag and thermal damping. *Journal of the Atmospheric Sciences*, 49, 861–878. https://doi.org/10.1175/1520-0469(1992)049<0861:NBIOTS>2.0.CO;2.

Batchelor, G.K. (1953) *The Theory of Homogeneous Turbulence*. Cambridge University Press, Cambridge; New York, 197 pp.

Bengtsson, L., Hodges, K.I., Esch, M., Keenlyside, N., Kornblueh, L., Luo, J.-J. and Yamagata, T. (2007) How may tropical cyclones change in a warmer climate? *Tellus A*, 59, 539–561. https://doi.org/10.1111/j.1600-0870.2007.00251.x.

Bengtsson, L., Hodges, K.I. and Keenlyside, N. (2009) Will extratropical storms intensify in a warmer climate? *Journal of Climate*, 22, 2276–2301. https://doi.org/10.1175/2008JCLI2678.1.

Blackmon, M.L. (1976) A climatological spectral study of the 500 mb geopotential height of the Northern Hemisphere. *Journal of the Atmospheric Sciences*, 33, 1607–1623. https://doi.org/10.1175/1520-0469(1976)033<1607:ACSSOT>2.0.CO;2.

Blackmon, M.L., Wallace, J.M., Lau, N.-C. and Mullen, S.L. (1977) An observational study of the Northern Hemisphere wintertime circulation. *Journal of the Atmospheric Sciences*, 34, 1040–1053. https://doi.org/10.1175/1520-0469(1977)034<1040:AOSOTN>2.0.CO;2.

Blackmon, M.L., Lee, Y.-H. and Wallace, J.M. (1984) Horizontal structure of 500 mb height fluctuations with long, intermediate and short time scales. *Journal of the Atmospheric Sciences*, 41, 961–980. https://doi.org/10.1175/1520-0469(1984)041<0961:HSOMHF>2.0.CO;2.

Brayshaw, D.J., Hoskins, B. and Blackburn, M. (2008) The storm-track response to idealized SST perturbations in an aquaplanet GCM. *Journal of the Atmospheric Sciences*, 65, 2842–2860. https://doi.org/10.1175/2008JAS2657.1.

Burrows, D.A., Chen, G. and Sun, L. (2017) Barotropic and baroclinic eddy feedbacks in the midlatitude jet variability and responses to climate change–like thermal forcings. *Journal of the Atmospheric Sciences*, 74, 111–132. https://doi.org/10.1175/JAS-D-16-0047.1.

Cai, M. and Mak, M. (1990) On the basic dynamics of regional cyclogenesis. *Journal of the Atmospheric Sciences*, 47, 1417–1442. https://doi.org/10.1175/1520-0469(1990)047<1417:OTBDOR>2.0.CO;2.

Catto, J.L., Shaffrey, L.C. and Hodges, K.I. (2010) Can climate models capture the structure of extratropical cyclones? *Journal of Climate*, 23, 1621–1635. https://doi.org/10.1175/2009JCLI3318.1.

Chang, E.K.M. (1993) Downstream development of baroclinic waves as inferred from regression analysis. *Journal of the Atmospheric Sciences*, 50, 2038–2053. https://doi.org/10.1175/1520-0469(1993)050<2038:DDOBWA>2.0.CO;2.

Chang, E.K.M. (2001a) GCM and observational diagnoses of the seasonal and interannual variations of the Pacific storm track during the cool season. *Journal of the Atmospheric Sciences*, 58, 1784–1800. https://doi.org/10.1175/1520-0469(2001)058<1784:GAODOT>2.0.CO;2.

Chang, E.K.M. (2001b) The structure of baroclinic wave packets. *Journal of the Atmospheric Sciences*, 58, 1694–1713. https://doi.org/10.1175/1520-0469(2001)058<1694:TSOBWP>2.0.CO;2.

Chang, E.K.M. and Orlanski, I. (1993) On the dynamics of a storm track. *Journal of the Atmospheric Sciences*, 50, 999–1015. https://doi.org/10.1175/1520-0469(1993)050<0999:OTDOAS>2.0.CO;2.

Chang, E.K.M., Lee, S. and Swanson, K.L. (2002) Storm track dynamics. *Journal of Climate*, 15, 2163–2183. https://doi.org/10.1175/1520-0442(2002)015<02163:STD>2.0.CO;2.

Charney, J.G. and Drazin, P.G. (1961) Propagation of planetary-scale disturbances from the lower into the upper atmosphere. *Journal of Geophysical Research*, 66, 83–109. https://doi.org/10.1029/JZ066i001p00083.

Chen, G. and Plumb, R.A. (2009) Quantifying the eddy feedback and the persistence of the zonal index in an idealized atmospheric model. *Journal of the Atmospheric Sciences*, 66, 3707–3720. https://doi.org/10.1175/2009JAS3165.1.

Dacre, H.F., Hawcroft, M.K., Stringer, M.A. and Hodges, K.I. (2012) An extratropical cyclone atlas: a tool for illustrating cyclone structure and evolution characteristics. *Bulletin of the American Meteorological Society*, 93, 1497–1502. https://doi.org/10.1175/BAMS-D-11-00164.1.

Deng, Y. and Mak, M. (2006) Nature of the differences in the intraseasonal variability of the Pacific and Atlantic storm tracks: a diagnostic study. *Journal of the Atmospheric Sciences*, 63, 2602–2615. https://doi.org/10.1175/JAS3749.1.

Dickinson, R.E. (1969) Theory of planetary wave-zonal flow interaction. *Journal of the Atmospheric Sciences*, 26, 73–81. https://doi.org/10.1175/1520-0469(1969)026<0073:TOPWZF>2.0.CO;2.

Eady, E.T. (1949) Long waves and cyclone waves. *Tellus*, 1(3), 33–52. https://doi.org/10.3402/tellusa.v1i3.8507.

Edmon, H.J., Hoskins, B.J. and McIntyre, M.E. (1980) Eliassen-Palm cross sections for the troposphere. *Journal of the Atmospheric Sciences*, 37, 2600–2616. https://doi.org/10.1175/1520-0469(1980)037<2600:EPCSFT>2.0.CO;2.

Eliassen, A. and Palm, E. (1961) On the transfer of energy in stationary mountain waves. *Geofysiske Publikasjoner*, 22, 1–23.

Farrell, B. (1984) Modal and non-modal baroclinic waves. *Journal of the Atmospheric Sciences*, 41, 668–673. https://doi.org/10.1175/1520-0469(1984)041<0668:MANMBW>2.0.CO;2.

Farrell, B. (1985) Transient growth of damped baroclinic waves. *Journal of the Atmospheric Sciences*, 42, 2718–2727. https://doi.org/10.1175/1520-0469(1985)042<2718:TGODBW>2.0.CO;2.

Farrell, B. (1989) Optimal excitation of baroclinic waves. *Journal of the Atmospheric Sciences*, 46, 1193–1206. https://doi.org/10.1175/1520-0469(1989)046<1193:OEOBW>2.0.CO;2.

Field, P.R. and Wood, R. (2007) Precipitation and cloud structure in midlatitude cyclones. *Journal of Climate*, 20, 233–254. https://doi.org/10.1175/JCLI3998.1.

Franzke, C., Woollings, T. and Martius, O. (2011) Persistent circulation regimes and preferred regime transitions in the North Atlantic. *Journal of the Atmospheric Sciences*, 68, 2809–2825. https://doi.org/10.1175/JAS-D-11-046.1.

Gerber, E.P. and Vallis, G.K. (2007) Eddy–zonal flow interactions and the persistence of the zonal index. *Journal of the Atmospheric Sciences*, 64, 3296–3311. https://doi.org/10.1175/JAS4006.1.

Green, J.S.A. (1960) A problem in baroclinic stability. *Quarterly Journal of the Royal Meteorological Society*, 86, 237–251. https://doi.org/10.1002/qj.49708636813.

Harnik, N. and Chang, E.K.M. (2004) The effects of variations in jet width on the growth of baroclinic waves: implications for midwinter Pacific storm track variability. *Journal of the Atmospheric Sciences*, 61, 23–40. https://doi.org/10.1175/1520-0469(2004)061<0023:TEOVIJ>2.0.CO;2.

Hartmann, D.L. (1974) Time spectral analysis of mid-latitude disturbances. *Monthly Weather Review*, 102, 348–362. https://doi.org/10.1175/1520-0493(1974)102<0348:TSAOML>2.0.CO;2.

Hodges, K.I. (1995) Feature tracking on the unit sphere. *Monthly Weather Review*, 123, 3458–3465. https://doi.org/10.1175/1520-0493(1995)123<3458:FTOTUS>2.0.CO;2.

Hoskins, B.J. and Hodges, K.I. (2002) New perspectives on the northern hemisphere winter storm tracks. *Journal of the Atmospheric Sciences*, 59, 1041–1061. https://doi.org/10.1175/1520-0469(2002)059<1041:NPOTNH>2.0.CO;2.

Hoskins, B.J. and Valdes, P.J. (1990) On the existence of storm-tracks. *Journal of the Atmospheric Sciences*, 47, 1854–1864. https://doi.org/10.1175/1520-0469(1990)047<1854:OTEOST>2.0.CO;2.

Hoskins, B.J., McIntyre, M.E. and Robertson, A.W. (1985) On the use and significance of isentropic potential vorticity maps. *Quarterly Journal of the Royal Meteorological Society*, 111, 877–946. https://doi.org/10.1002/qj.49711147002.

Kidston, J. and Vallis, G.K. (2012) The relationship between the speed and the latitude of an eddy-driven jet in a stirred barotropic model. *Journal of the Atmospheric Sciences*, 69, 3251–3263. https://doi.org/10.1175/JAS-D-11-0300.1.

Kidston, J., Frierson, D.M.W., Renwick, J.A. and Vallis, G.K. (2010) Observations, simulations, and dynamics of jet stream variability and annular modes. *Journal of Climate*, 23, 6186–6199. https://doi.org/10.1175/2010JCLI3235.1.

Lau, N.-C. (1979) The structure and energetics of transient disturbances in the Northern Hemisphere wintertime circulation. *Journal of the Atmospheric Sciences*, 36, 982–995. https://doi.org/10.1175/1520-0469(1979)036<0982:TSAEOT>2.0.CO;2.

Lee, S. and Kim, H. (2003) The dynamical relationship between subtropical and eddy-driven jets. *Journal of the Atmospheric Sciences*, 60, 1490–1503. https://doi.org/10.1175/1520-0469(2003)060<1490:TDRBSA>2.0.CO;2.

Li, C. and Wettstein, J.J. (2011) Thermally driven and eddy-driven jet variability in reanalysis. *Journal of Climate*, 25, 1587–1596. https://doi.org/10.1175/JCLI-D-11-00145.1.

Liang, X.S. (2016) Canonical transfer and multiscale energetics for primitive and quasigeostrophic atmospheres. *Journal of the Atmospheric Sciences*, 73, 4439–4468. https://doi.org/10.1175/JAS-D-16-0131.1.

Liang, X.S. and Anderson, D.G.M. (2007) Multiscale window transform. *Multiscale Modeling and Simulation*, 6, 437–467. https://doi.org/10.1137/06066895X.

Liang, X.S. and Robinson, A.R. (2005) Localized multiscale energy and vorticity analysis: I. Fundamentals. *Dynamics of Atmospheres and Oceans*, 38, 195–230. https://doi.org/10.1016/j.dynatmoce.2004.12.004.

Liang, X.S. and Robinson, A.R. (2007) Localized multi-scale energy and vorticity analysis: II. Finite-amplitude instability theory and validation. *Dynamics of Atmospheres and Oceans*, 44, 51–76. https://doi.org/10.1016/j.dynatmoce.2007.04.001.

Lim, G.H. and Wallace, J.M. (1991) Structure and evolution of baroclinic waves as inferred from regression analysis. *Journal of the Atmospheric Sciences*, 48, 1718–1732. https://doi.org/10.1175/1520-0469(1991)048<1718:SAEOBW>2.0.CO;2.

Lindzen, R.S. and Farrell, B. (1980) A simple approximate result for the maximum growth rate of baroclinic instabilities. *Journal of the Atmospheric Sciences*, 37, 1648–1654. https://doi.org/10.1175/1520-0469(1980)037<1648:ASARFT>2.0.CO;2.

Lindzen, R.S. and Holton, J.R. (1968) A theory of the quasi-biennial oscillation. *Journal of the Atmospheric Sciences*, 25, 1095–1107. https://doi.org/10.1175/1520-0469(1968)025<1095:ATOTQB>2.0.CO;2.

Lorenz, E.N. (1955) Available potential energy and the maintenance of the general circulation. *Tellus*, 7, 157–167. https://doi.org/10.1111/j.2153-3490.1955.tb01148.x.

Lorenz, D.J. (2014) Understanding midlatitude jet variability and change using Rossby wave chromatography: wave–mean flow interaction. *Journal of the Atmospheric Sciences*, 71, 3684–3705. https://doi.org/10.1175/JAS-D-13-0201.1.

Lorenz, D.J. and Hartmann, D.L. (2001) Eddy–zonal flow feedback in the Southern Hemisphere. *Journal of the Atmospheric Sciences*, 58, 3312–3327. https://doi.org/10.1175/1520-0469(2001)058<3312:EZFFIT>2.0.CO;2.

Ma, J. and Liang, X.S. (2017) Multiscale dynamical processes underlying the wintertime Atlantic blockings. *Journal of the Atmospheric Sciences*, 74, 3815–3831.

Mak, M. and Cai, M. (1989) Local barotropic instability. *Journal of the Atmospheric Sciences*, 46, 3289–3311. https://doi.org/10.1175/1520-0469(1989)046<3289:LBI>2.0.CO;2.

Nakamura, H. (1992) Midwinter suppression of baroclinic wave activity in the Pacific. *Journal of the Atmospheric Sciences*, 49, 1629–1642. https://doi.org/10.1175/1520-0469(1992)049<1629:MSOBWA>2.0.CO;2.

Novak, L., Ambaum, M.H.P. and Tailleux, R. (2015) The life cycle of the North Atlantic storm track. *Journal of the Atmospheric Sciences*, 72, 821–833. https://doi.org/10.1175/JAS-D-14-0082.1.

Orlanski, I. and Chang, E.K.M. (1993) Ageostrophic geopotential fluxes in downstream and upstream development of baroclinic waves. *Journal of the Atmospheric Sciences*, 50, 212–225. https://doi.org/10.1175/1520-0469(1993)050<0212:AGFIDA>2.0.CO;2.

Orlanski, I. and Katzfey, J. (1991) The life cycle of a cyclone wave in the Southern Hemisphere. Part I: eddy energy budget. *Journal of the Atmospheric Sciences*, 48, 1972–1998. https://doi.org/10.1175/1520-0469(1991)048<1972:TLCOAC>2.0.CO;2.

Papritz, L. and Schemm, S. (2013) Development of an idealised downstream cyclone: Eulerian and Lagrangian perspective on the kinetic energy. *Tellus A*, 65, 19539. https://doi.org/10.3402/tellusa.v65i0.19539.

Penny, S.M., Battisti, D.S. and Roe, G.H. (2013) Examining mechanisms of variability within the Pacific storm track: upstream seeding and jet-core strength. *Journal of Climate*, 26, 5242–5259. https://doi.org/10.1175/JCLI-D-12-00017.1.

Pierrehumbert, R.T. and Swanson, K.L. (1995) Baroclinic instability. *Annual Review of Fluid Mechanics*, 27, 419–467. https://doi.org/10.1146/annurev.fl.27.010195.002223.

Plumb, R.A. (1983) A new look at the energy cycle. *Journal of the Atmospheric Sciences*, 40, 1669–1688. https://doi.org/10.1175/1520-0469(1983)040<1669:ANLATE>2.0.CO;2.

Plumb, R.A. (1985) An alternative form of Andrews' conservation law for quasi-geostrophic waves on a steady, nonuniform flow. *Journal of the Atmospheric Sciences*, 42, 298–300. https://doi.org/10.1175/1520-0469(1985)042<0298:AAFOAC>2.0.CO;2.

Rivière, G., Hua, B.L. and Klein, P. (2003) Perturbation growth in terms of barotropic alignment properties. *Quarterly Journal of the Royal Meteorological Society*, 129, 2613–2635. https://doi.org/10.1256/qj.02.106.

Rivière, G., Hua, B.L. and Klein, P. (2004) Perturbation growth in terms of baroclinic alignment properties. *Quarterly Journal of the Royal Meteorological Society*, 130, 1655–1673. https://doi.org/10.1256/qj.02.223.

Rivière, G., Arbogast, P. and Joly, A. (2015) Eddy kinetic energy redistribution within idealized extratropical cyclones using a two-layer quasi-geostrophic model. *Quarterly Journal of the Royal Meteorological Society*, 141, 207–223. https://doi.org/10.1002/qj.2350.

Robinson, W.A. (2000) A baroclinic mechanism for the eddy feedback on the zonal index. *Journal of the Atmospheric Sciences*, 57, 415–422. https://doi.org/10.1175/1520-0469(2000)057<0415:ABMFTE>2.0.CO;2.

Simmons, A.J. and Hoskins, B.J. (1978) The life cycles of some nonlinear baroclinic waves. *Journal of the Atmospheric Sciences*, 35, 414–432. https://doi.org/10.1175/1520-0469(1978)035<0414:TLCOSN>2.0.CO;2.

Simmons, A.J. and Hoskins, B.J. (1980) Barotropic influences on the growth and decay of nonlinear baroclinic waves. *Journal of the Atmospheric Sciences*, 37, 1679–1684. https://doi.org/10.1175/1520-0469(1980)037<1679:BIOTGA>2.0.CO;2.

Sinclair, M.R. and Revell, M.J. (2000) Classification and composite diagnosis of extratropical cyclogenesis events in the southwest Pacific. *Monthly Weather Review*, 128, 1089–1105. https://doi.org/10.1175/1520-0493(2000)128<1089:CACDOE>2.0.CO;2.

Strang, G. and Nguyen, T. (1996) *Wavelets and Filter Banks*, 2nd edition. Wellesley, MA: Wellesley-Cambridge Press, 520 pp.

Uppala, S.M., Kållberg, P.W., Simmons, A.J., Andrae, U., Bechtold, V.D.C., Fiorino, M., Gibson, J.K., Haseler, J., Hernandez, A., Kelly, G.A., Li, X., Onogi, K., Saarinen, S., Sokka, N., Allan, R.P., Andersson, E., Arpe, K., Balmaseda, M.A., Beljaars, A.C.M., Berg, L.V.D., Bidlot, J., Bormann, N., Caires, S., Chevallier, F., Dethof, A., Dragosavac, M., Fisher, M., Fuentes, M., Hagemann, S., Hólm, E., Hoskins, B.J., Isaksen, L., Janssen, P.A.E.M., Jenne, R., Mcnally, A.P., Mahfouf, J.-F., Morcrette, J.-J., Rayner, N.A., Saunders, R.W., Simon, P., Sterl, A., Trenberth, K.E., Untch, A., Vasiljevic, D., Viterbo, P. and Woollen, J. (2005) The ERA-40 re-analysis. *Quarterly Journal of the Royal Meteorological Society*, 131, 2961–3012. https://doi.org/10.1256/qj.04.176.

Vallis, G.K. and Gerber, E.P. (2008) Local and hemispheric dynamics of the North Atlantic Oscillation, annular patterns and the zonal index. *Dynamics of Atmospheres and Oceans*, 44, 184–212. https://doi.org/10.1016/j.dynatmoce.2007.04.003.

Woollings, T., Hannachi, A. and Hoskins, B. (2010) Variability of the North Atlantic eddy-driven jet stream. *Quarterly Journal of the Royal Meteorological Society*, 136, 856–868. https://doi.org/10.1002/qj.625.

Xu, F. and Liang, X.S. (2017) On the generation and maintenance of the 2012/13 sudden stratospheric warming. *Journal of the Atmospheric Sciences*, 74, 3209–3228.

Zhang, Y., Yang, X.-Q., Nie, Y. and Chen, G. (2012) Annular mode-like variation in a multilayer quasigeostrophic model. *Journal of the Atmospheric Sciences*, 69, 2940–2958. https://doi.org/10.1175/JAS-D-11-0214.1.

Zhao, Y.-B. and Liang, X.S. (2018) On the inverse relationship between the boreal wintertime Pacific jet strength and storm-track intensity. *Journal of Climate*, 31, 9545–9564. https://doi.org/10.1175/JCLI-D-18-0043.1.

Zhao, Y.-B., Liang, X.S. and Zhu, W. (2018) Differences in storm structure and internal dynamics of the two storm source regions over East Asia. *Acta Meteorologica Sinica*, 76, 663–679. https://doi.org/10.11676/qxxb2018.033.

SUPPORTING INFORMATION

Additional supporting information may be found online in the Supporting Information section at the end of the article.

How to cite this article: Zhao Y-B, Liang XS, Guan Z, Hodges KI. The asymmetric eddy–background flow interaction in the North Pacific storm track. *Q J R Meteorol Soc* 2019;145:575–596. https://doi.org/10.1002/qj.3453

APPENDIX: A BRIEF INTRODUCTION OF THE MULTISCALE WINDOW TRANSFORM, CANONICAL TRANSFER, AND THE LOCAL LORENZ CYCLE

In this appendix, we present the mathematical formulas required for the analysis. A detailed introduction of the methodologies is beyond scope here; for that we refer readers to Liang (2016) and Liang and Anderson (2007). In Xu and Liang (2017), there is a brief comparison with the traditional energetics in the Reynolds framework.

Multiscale window transform

As is well known, multiscale energetics formulated with the time mean (resp., zonal mean) do not have information on time (resp., longitude). These formalisms, or Reynolds decomposition-based formalisms as they are known, cannot be used to study the energy burst processes which are generally localized in space and time. During past decades, it was common practice to use filtering to replace the time-averaging in these formalisms. For example, application of a low-pass filter to a velocity field $u(t)$ yields a slowly varying $\overline{u}(t)$, and a high-pass filter to it gives a fast-varying eddy part $u'(t)$: $u(t) = \overline{u}(t) + u'(t)$. Now time dependence is retained in both fields, and thus seemingly the local information is retained. This entails a very basic physical question: What are the mean energy and the eddy energy with this decomposition? When $\overline{u}$ is time invariant, this is a Reynolds decomposition, and we know that the eddy energy is $\overline{[u'(t)]^2}$. Now if $\overline{u}$ is time varying, what is the eddy energy then? During the past two or three decades, a common practice in the literature was to simply take it as $[u'(t)]^2$. This corresponds, in the Reynolds decomposition case, to a relieving of the time mean in the eddy energy $\overline{[u'(t)]^2}$.

This is unfortunately conceptually incorrect. To illustrate this, consider a very simple example which has a Fourier expansion

$$u(t) = \overline{u}(t) + u'(t) = [a_0 \cos \omega_0 t] + [a_1 \cos \omega_1 t], \quad \omega_1 > \omega_0,$$

with subscripts 0 and 1 representing the slow and fast processes, respectively. Now what are the energies for these processes? In this simple case we know that they should be a_0^2 and a_1^2, respectively. That is to say that multiscale energy is a concept in phase space; here they are functions of the Fourier coefficients (a_0, a_1). By the common practice using filters as shown above, however, the energies would simply be taken as

$$[\overline{u}(t)]^2 = [a_0 \cos \omega_0 t]^2 \text{ and } [u'(t)]^2 = [a_1 \cos \omega_1 t]^2,$$

which are functions of the reconstructions or filtered parts in physical space!

So the common practice employed during the past decades is conceptually incorrect. Multiscale energy is a concept in phase space; it is related to its physical space counterpart through the famous Parseval equality. Mathematically, it is the square of the norm of a field variable, or, alternatively, the Fourier transform of an autocorrelation function (e.g., Batchelor, 1953). In the above example, when $\omega_0 = 0$, it is easy to prove that $a_1{}^2 = \overline{[u'(t)]^2}$, just as for the case with the Reynolds decomposition. From this example one also sees that the time mean in the classical Reynolds formalism is essential; *it cannot be removed to feign the gain of the time variability*. In fact, it is by no means a trivial task to have the local energy of a time-dependent filtered field faithfully represented; it is a rather profound problem. This was not even made possible until filter banks and wavelets were connected (Strang and Nguyen, 1996), and was only systematically addressed by Liang and Anderson (2007) in the development of the multiscale window transform (MWT).

The MWT is a tool that helps to decompose a function space into a direct sum of orthogonal subspaces, each with an exclusive range of scales (represented by wavelet scale levels), while having the local information retained. Such a subspace is termed a *scale window*, or simply a window. The MWT can be viewed as a generalization of the classical Reynolds decomposition; it was originally developed for representing energies (and any quadratic quantities) on the resulting scale windows, in order to make the analysis of multiscale energetics possible. Liang and Anderson (2007) found that, for some specially constructed orthogonal[9] filters, there exists a transfer–reconstruction pair, namely MWT and its counterpart multiscale window reconstruction (MWR). In some sense MWR functions just like a filter in the traditional sense. What makes it different is that, for each MWR, there exists an MWT that gives coefficients which can be used to represent the energy of the filtered series. In this way multiscale energetics analysis is made possible.

In MWT, a scale window is demarcated by two scale levels, or window bounds. For a time series with a duration τ, a scale level j corresponds to a period $2^{-j}\tau$. In the M-window case, the windows are bounded above by $M + 1$ scale levels: $j_0, j_1, \ldots, j_M$. Alternatively, $2^{-j_0}\tau, 2^{-j_1}\tau, \ldots, 2^{-j_M}\tau$ are the time-scale bounds. For convenience, we will denote them by $\varpi = 0, 1, \ldots, M$, respectively.

[9]Note here that *orthogonality* is crucial, otherwise Parseval's relation does not hold and the energy cannot even be defined.

Now suppose that $\{\phi_n^j(t)\}_n$ is an orthonormal translational invariant scaling sequence (built from cubic splines; see Liang and Anderson [2007] and Figure 1 in Liang [2016]), with j some wavelet scale level and n the time step. Let $T(t)$ be some square integrable function defined on [0,1] (if not, the domain can always be rescaled to [0,1]). It has been shown (Liang and Anderson, 2007) that all such functions can be practically represented using $\{\phi_n^j(t)\}_n$ as a basis. In doing so, there is a scaling transform

$$\hat{T}_n^j = \int_0^1 T(t)\phi_n^j(t)dt$$

for any scale level j (corresponding to frequency 2^j). Given the window bounds j_0, j_1 for a two-window decomposition, T then can be reconstructed on the windows formed above:

$$T^{\sim 0}(t) = \sum_{n=0}^{2^{j_0}-1} \hat{T}_n^{j_0}\phi_n^{j_0}(t),$$

$$T^{\sim 1}(t) = \sum_{n=0}^{2^{j_1}-1} \hat{T}_n^{j_1}\phi_n^{j_1}(t) - T^{\sim 0}(t),$$

with the notation ~ 0, ~ 1 signifying the corresponding scale windows. With these reconstructions (multiscale window reconstructions, i.e., MWR), the MWT of T is defined as

$$\hat{T}_n^{\sim\varpi} = \int_0^1 T^{\sim\varpi}(t)\phi_n^{j_1}(t)dt$$

for windows $\varpi = 0, 1, n = 0, 1, \ldots, N$ and $N = 2^{j_1} - 1$. In terms of $\hat{T}^{\sim\varpi}$ the above reconstructions on the two windows can be written in a unified way:

$$T^{\sim\varpi}(t) = \sum_{n=0}^{2^{j_1}-1} \hat{T}_n^{\sim\varpi}\phi_n^{j_1}(t).$$

These two equations make a transform–reconstruction pair for the MWT. Note that the $T^{\sim\varpi}(t)$ are just like the low-/high-pass filtered quantities defined in physical space, while the transform coefficients $\hat{T}_n^{\sim\varpi}$ (just like the Fourier coefficients) can be used to represent multiscale energy – it has been rigorously proved that the energy on scale ϖ is precisely equal to the square of the MWT coefficients (up to some constant multiplier). Note that it is by no means as trivial as $[T^{\sim\varpi}(t)]^2$, which has frequently been seen in the literature.

Multiscale energetics and the local Lorenz cycle

Following Liang (2016), consider the primitive equations in an isobaric coordinate frame:

$$\frac{\partial \mathbf{v}_h}{\partial t} + \mathbf{v}_h \cdot \nabla_h \mathbf{v}_h + \omega\frac{\partial \mathbf{v}_h}{\partial p} + f\mathbf{k}\times\mathbf{v}_h = -\nabla_h\Phi + \mathbf{F}, \quad \text{(A1)}$$

$$\frac{\partial \Phi}{\partial p} = -\alpha, \quad \text{(A2)}$$

$$\nabla_h \cdot \mathbf{v}_h + \frac{\partial \omega}{\partial p} = 0, \quad \text{(A3)}$$

$$\frac{\partial T}{\partial t} + \mathbf{v}_h \cdot \nabla_h \mathrm{T} + \omega\frac{\partial T}{\partial p} + \omega\bar{\alpha}\frac{L - L_d}{g} + \omega\alpha\frac{L - L_d}{g} = \frac{\dot{q}_{net}}{c_p}, \quad \text{(A4)}$$

$$p\alpha = RT, \quad \text{(A5)}$$

where L is the lapse rate and L_d is the lapse rate for dry air, the subscript h stands for horizontal direction and the overbar represents the mean over time and over the isobaric plane. Other notation is conventional. Note here that Φ (geopotential) and α (specific volume) are anomalies; their time-averages have been pre-subtracted.

With MWT, the APE and KE densities on window ϖ at location n can be defined, following Lorenz (1955), as

$$A^{\varpi} = \frac{1}{2}c(\hat{T}^{\sim\varpi})^2, \quad \text{(A6)}$$

$$K^{\varpi} = \frac{1}{2}\hat{\mathbf{v}}_{\mathrm{h}}^{\sim\varpi} \cdot \hat{\mathbf{v}}_{\mathrm{h}}^{\sim\varpi}. \quad \text{(A7)}$$

Note here that the subscript n has been suppressed for clarity, the same as below. From Equations A1–A5 the evolutionary equations for A^{ϖ} and K^{ϖ} for windows ϖ (=0, 1, …) can be obtained; they are Equations 1 and 2, which we rewrite as follows:

$$\frac{\partial A^{\varpi}}{\partial t} + \nabla \cdot \mathbf{Q}_A^{\varpi} = \Gamma_A^{\varpi} - b^{\varpi} + \mathrm{S}_A^{\varpi} + \mathrm{F}_A^{\varpi}, \quad \text{(A8)}$$

$$\frac{\partial K^{\varpi}}{\partial t} + \nabla \cdot \mathbf{Q}_K^{\varpi} = \Gamma_K^{\varpi} - \nabla \cdot \mathbf{Q}_P^{\varpi} + b^{\varpi} + \mathrm{F}_K^{\varpi}. \quad \text{(A9)}$$

The physical explanations and mathematical expressions for these terms are listed in Table A1.

Among the terms in Table A1 are Γ_A^{ϖ} and Γ_K^{ϖ}, which represent the transfers of APE and KE between the scale windows and hence make the processes that we are most interested in for this study. For a scalar field T (which may be any scalar field or component of a vector field, not necessarily temperature) in a flow $\boldsymbol{v}$, the energy transfer from the other scale windows to window ϖ is (see Liang [2016] for a rigorous proof)

$$\Gamma_n^{\varpi} = -E_n^{\varpi}\nabla \cdot \mathbf{v}_{\mathrm{T}}^{\varpi} = \frac{1}{2}[\widehat{(\mathbf{v}T)}_n^{\sim\varpi} \cdot \nabla\hat{T}_n^{\sim\varpi} - \hat{T}_n^{\sim\varpi}\nabla \cdot \widehat{(\mathbf{v}T)}_n^{\sim\varpi}], \quad \text{(A10)}$$

where $E^{\varpi} = \frac{1}{2}(\hat{T}^{\sim\varpi})^2$ is the energy of window ϖ.[10] The other symbol,

$$\mathbf{v}_{\mathrm{T}}^{\varpi} = \frac{\widehat{(T\mathbf{v})}_n^{\sim\varpi}}{\hat{T}_n^{\sim\varpi}}, \quad \text{(A11)}$$

is referred to as the *T-coupled velocity*, which can be understood as the weighted average of $\boldsymbol{v}$ in the phase space of MWT. With this, the transfer of APE and KE can be easily obtained. For example,

$$\Gamma_{\mathrm{K}}^{\varpi} = -\frac{1}{2}[(\hat{u}^{\sim\varpi})^2\nabla \cdot \mathbf{v}_{\mathrm{u}}^{\varpi} + (\hat{v}^{\sim\varpi})^2\nabla \cdot \mathbf{v}_{\mathrm{v}}^{\varpi}], \quad \text{(A12)}$$

which can be proved to be that in Table A1.

The so-obtained transfer possesses a very interesting property, namely

$$\sum_{\varpi}\sum_{n}\Gamma_n^{\varpi} = 0, \quad \text{(A13)}$$

[10] When required, a constant should be multiplied on both sides. For example, if T is temperature, then E^{ϖ} and Γ^{ϖ} should both be multiplied by c to make APE and APE transfer.

TABLE A1 The energetic terms in Equations A8 and A9. The colon operator (:) in Γ_K^{ϖ} and Γ_A^{ϖ} is defined such that, for two dyadic products **AB** and **CD**, $(\mathbf{AB}):(\mathbf{CD})=(\mathbf{A}\cdot\mathbf{C})(\mathbf{B}\cdot\mathbf{D})$. If the total energetics (in W) are to be computed, the resulting integrals with respect to (x, y, p) should be divided by g. Besides, all terms are to be multiplied by 2^{j_1}, which is omitted for notational simplicity

Symbol	Mathematical expression	Physical interpretation
K^{ϖ}	$\frac{1}{2}\hat{\mathbf{v}}_h^{\sim\varpi}\cdot\hat{\mathbf{v}}_h^{\sim\varpi}$	KE on scale window ϖ
$\boldsymbol{Q}_K^{\varpi}$	$\frac{1}{2}\widehat{(\mathbf{v}\mathbf{v}_h)}^{\sim\varpi}\cdot\hat{\mathbf{v}}_h^{\sim\varpi}$	Flux of KE on window ϖ
Γ_K^{ϖ}	$\frac{1}{2}[\widehat{(\mathbf{v}\mathbf{v}_h)}^{\sim\varpi}:\nabla\hat{\mathbf{v}}_h^{\sim\varpi}-\nabla\cdot\widehat{(\mathbf{v}\mathbf{v}_h)}^{\sim\varpi}\cdot\hat{\mathbf{v}}_h^{\sim\varpi}]$	Canonical transfer of KE to window ϖ
$\boldsymbol{Q}_P^{\varpi}$	$\hat{\mathbf{v}}^{\sim\varpi}\hat{\Phi}^{\sim\varpi}$	Geopotential flux
b^{ϖ}	$-\widehat{\omega}^{\sim\varpi}\widehat{\alpha}^{\sim\varpi}$	Buoyancy conversion
A^{ϖ}	$\frac{1}{2}c(\hat{\mathrm{T}}^{\sim\varpi})^2, c=\frac{g}{\overline{T}(g/C_p-L)}$	APE on scale window ϖ
$\boldsymbol{Q}_A^{\varpi}$	$\frac{1}{2}c\hat{\mathrm{T}}^{\sim\varpi}\widehat{(\mathbf{v}\mathrm{T})}^{\sim\varpi}$	Flux of APE on window ϖ
Γ_A^{ϖ}	$\frac{c}{2}[\widehat{(\mathbf{v}\mathrm{T})}^{\sim\varpi}\cdot\nabla\hat{\mathrm{T}}^{\sim\varpi}-\hat{\mathrm{T}}^{\sim\varpi}\nabla\cdot\widehat{(\mathbf{v}\mathrm{T})}^{\sim\varpi}]$	Canonical transfer of APE to window ϖ
S_A^{ϖ}	$\frac{1}{2}\hat{\mathrm{T}}^{\sim\varpi}\widehat{(\omega T)}^{\sim\varpi}\frac{\partial c}{\partial p}+\frac{1}{\overline{T}}\widehat{\omega\alpha}^{\sim\varpi}$	Apparent source/sink (usually negligible)

as first proposed in Liang and Robinson (2005) and later proved in Liang (2016). Physically, this implies that the transfer is a mere redistribution of energy among the scale windows, without generating or destroying the energy as a whole. This property, although simple to state, does not hold in previous time decomposition-based or Lorenz-type energetics formalisms (refer to Liang and Robinson [2007] for a clear comparison to the classical formalism). To distinguish it from those that may have been encountered in the literature, it is termed the *canonical transfer*.

As shown in Liang (2016), a canonical transfer has a *Lie bracket form*; it satisfies the *Jacobian identity*, reminiscent of the *Poisson bracket in Hamiltonian mechanics*. It also satisfies a *detailed balance relation*, which usually results from Saltzman-type or space decomposition-based energetics formalisms (Liang and Robinson, 2005).

So, for an ideal fluid, the energetic processes represented in Equations A8 and A9 are all conservative. In other words, a local Lorenz cycle in the absence of dissipation and diffusion is composed of the following three types of processes:

- Transports: redistributing energy in space (vanishing if integrated over a closed domain);
- Canonical transfers: redistributing energy among scale windows (vanishing if summarized over scale windows and locations);
- Buoyancy conversion: redistributing energy between APE and KE.

Figure A1 schematizes these processes for a two-window decomposition. Note here that the arrows connecting $K^0(A^0)$ and $K^1(A^1)$ are the quantities that are difficult to diagnose with traditional methods.

Note that a canonical transfer may involve contributions from essentially all scale windows; it is necessary to differentiate them. Consider, for example, window $\varpi=1$. The energy transferred to the window can be from window 0 and from itself $\varpi=1$. Since all canonical transfers are linear combinations of terms in a triple product form,

$$\Gamma_n^1=\hat{\mathcal{R}}_n^{\sim 1}\widehat{(pq)}_n^{\sim 1},$$

it suffices to consider Γ_n^1. From Liang (2016), it is

$$\Gamma_n^1=\hat{\mathcal{R}}_n^{\sim 1}[\widehat{(p^{\sim 0}q^{\sim 0})}_n^{\sim 1}+\widehat{(p^{\sim 0}q^{\sim 1})}_n^{\sim 1}+\widehat{(p^{\sim 1}q^{\sim 0})}_n^{\sim 1}]+\hat{\mathcal{R}}_n^{\sim 1}\widehat{(p^{\sim 1}q^{\sim 1})}_n^{\sim 1},$$

where the first part on the right-hand side is the canonical energy transfer from window 0 to window 1; write it as $\Gamma^{0\to 1}$. The second part, denoted by $\Gamma^{1\to 1}$, is the canonical energy transfer to itself, which is usually very small. $\Gamma^{0\to 1}$ is of particular importance in that it is usually related to the instability in geophysical fluid dynamics; in particular, $\Gamma_A^{0\to 1}$ and $\Gamma_K^{0\to 1}$ are usually related to the baroclinic instability and barotropic instability of the mean flow. For this reason, in the text sometimes $\Gamma_A^{0\to 1}$ and $\Gamma_K^{0\to 1}$ are referred to as the baroclinic canonical transfer and the barotropic canonical transfer, respectively.

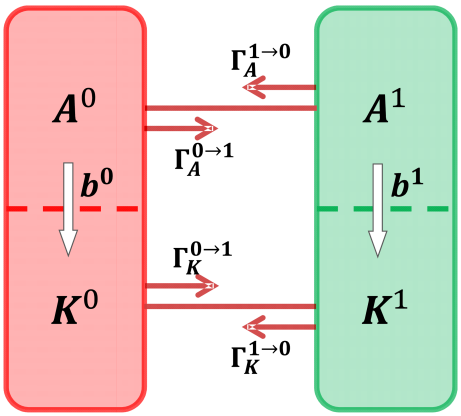

FIGURE A1 The local Lorenz cycle for a two-window decomposition (the scale windows are denoted in the superscripts as 0 and 1, respectively). For clarity, transports and dissipative/diffusive processes are not shown. [Colour figure can be viewed at wileyonlinelibrary.com].